OPTIMIZING OBSERVATIONS OF SUPERNOVA PECULIAR VELOCITIES

Karolina Torres Garcia

Dissertação de Mestrado apresentada ao Programa de Pós-Graduação em Astronomia da Universidade Federal do Rio de Janeiro - UFRJ, como parte dos requisitos necessários à obtenção do título de Mestre em Ciências (Astronomia).

Orientador: Miguel Boavista Quartin

Coorientadora: Beatriz Blanco Siffert

Rio de Janeiro

Abril de 2018

OPTIMIZING OBSERVATIONS OF SUPERNOVA PECULIAR VELOCITIES

Karolina Torres Garcia

Miguel Boavista Quartin

Beatriz Blanco Siffert

Dissertação de Mestrado submetida ao Programa de Pós-graduação em Astronomia, Observatório do Valongo, da Universidade Federal do Rio de Janeiro - UFRJ, como parte dos requisitos necessários à obtenção do título de Mestre em Astronomia.

Aprovada por:

Presidente, Prof.

Prof.

Prof.

Prof.

Rio de Janeiro

Abril de 2018

Garcia, Karolina Torres
G216o Optimizing observations of supernova peculiar velocities / Karolina Torres Garcia. - Rio de Janeiro: UFRJ/OV, 2018.
78 f.

Orientador: Miguel Boavista Quartin.
Coorientadora: Beatriz Blanco Siffert.
Dissertação (mestrado) - Universidade Federal do Rio de Janeiro, Observatório do Valongo, Programa de Pós-Graduação em Astronomia, 2018.

1. Supernovas do Tipo Ia. 2. Velocidades peculiares. 3. Parâmetros cosmológicos de perturbação. 4. Estratégias observacionais. I. Quartin, Miguel Boavista, orient. II. Siffert, Beatriz Blanco, coorient. III. Optimizing observations of supernova peculiar velocities.

Resumo

Otimizando observações de velocidades peculiares de supernovas

Karolina Torres Garcia

Orientador: Miguel Boavista Quartin

Coorientadora: Beatriz Blanco Siffert

As supernovas do Tipo Ia são fontes de informação muito importantes para a Cosmologia, visto que elas ainda são as únicas velas-padrão de alto redshift bem estabelecidas. A fim de estimar parâmetros cosmológicos com elas, precisamos levar em conta algumas fontes de incerteza, que incluem suas dispersões intrínsecas e velocidades peculiares, normalmente modeladas como termos gaussianos aleatórios. No entanto, o fato é que velocidades peculiares introduzem uma fonte de correlação entre magnitudes de supernovas que deve ser considerada em análises de amostras de baixo redshift. Isso significa que os resíduos do diagrama de Hubble contêm informações importantes sobre o espectro de potências de matéria atual (cuja amplitude é obtida analisando a função de correlação de dois pontos de velocidades peculiares de supernovas), e sobre a taxa de crescimento do Universo.

Nesse trabalho, nós estudamos supernovas do Tipo Ia de baixo redshift para entender como diferentes parâmetros observacionais (o tempo de observação, a área observada e o redshift alcançado) influenciam na estimação dos parâmetros de perturbação σ_8 e γ. σ_8 é um parâmetro que faz parte do modelo cosmológico padrão e representa o valor quadrático médio do contraste de matéria no Universo; ele proporciona informações acerca da formação de estruturas no regime linear - quanto maior seu valor, mais inomogêneo é o Universo. γ é o índice da taxa de crescimento relacionado com a parametrização do crescimento de estruturas no regime linear. Os dois parâmetros são usados também para testar a consistência do modelo cosmológico padrão.

Apesar de ser comum na literatura considerar que as contribuições das velocidades peculiares de supernovas para o erro total só são relevantes para supernovas até $z \approx 0,1$, nesse trabalho mostramos que é possível ganhar informação nas estimativas de σ_8 e γ indo até $z \approx 0,2$. Além disso, nós concluimos que o erro nesses vínculos para a nossa amostra cai como uma lei de potência com índice de $0,5$ em função da área coberta e que não segue uma lei de potência em função da duração do levantamento (o ganho de informação atinge um limite após certo tempo). Para a nossa amostra de 11285 supernovas cobrindo 600 graus^2 em 6 anos, nós concluimos que o levantamento se beneficiaria de observar por mais tempo o mesmo campo antes de mudar para uma outra área do céu. Fazendo uma análise preliminar do DES e do LSST, nós mostramos que os dois também deveriam preferir continuar no mesmo campo por mais tempo do que o previsto (5 anos para o DES e 10 para o LSST) para otimizar as observações de velocidades peculiares de supernovas.

Palavras-chave: Supernovas do Tipo Ia, velocidades peculiares, parâmetros cosmológicos de perturbação, estratégias observacionais.

Rio de Janeiro

Abril de 2018

Abstract

Optimizing Observations of Supernova Peculiar Velocities

Karolina Torres Garcia

Advisor: Miguel Boavista Quartin

Co-advisor: Beatriz Blanco Siffert

Type Ia supernovae are very important sources of information to Cosmology as they are still the only established high-redshift standard candles. In order to constrain cosmological parameters based on them, we need to account for some sources of uncertainty, including their intrinsic dispersions and peculiar velocities. These uncertainties are often just modeled as Gaussian random terms; however, supernova peculiar velocities introduce a source of correlation between supernova magnitudes that should be considered in all analyses of nearby samples. This implies that the supernova Hubble diagram residual contains valuable information on both the present matter power spectrum (whose amplitude is obtained by analyzing the 2-point correlation function of supernova peculiar velocities), and the growth rate of the Universe.

In this work, we study low-redshift Type Ia supernovae to understand how different survey parameters such as its duration, the area covered and the redshift reached influence on the estimation of the perturbation parameters σ_8 and γ. σ_8 is a parameter included in the standard model of cosmology that represents the mean square value of the matter contrast in the Universe and measures the formation of structures in the linear regime - the larger its value, the more inhomogeneous is the cosmos. γ is the growth rate index related to the common parametrization for the linear growth of structures. Both these parameters are also useful to test the consistency of the General Relativity and the standard model of cosmology.

Despite the common assumption that supernova peculiar velocities just relevantly contributes to the overall error budget when considering $z \lesssim 0.1$, in this work we show that it is possible to gain information on the estimation of σ_8 and γ by going until $z \approx 0.2$. In addition, we concluded that the error on those constraints for our sample falls as a power law with index 0.5 as a function of the area covered, and does not follow a power law as a function of survey duration (the gain of information reaches a limit after a determined time). For our 11,285-supernova 600-deg^2 sample that lasts 6 years, we concluded that the survey would benefit more from staying longer in the same field before exploring another area of the sky. Making a preliminary analysis for the Dark Energy Survey (DES) and the Large Synoptic Survey Telescope (LSST), we show that they both also should prefer staying longer in the same area then the intended time (5 years for DES and 10 years for LSST) to optimize observations of supernova peculiar velocities.

Keywords: Type Ia supernovae, peculiar velocities, perturbation cosmological parameters, observational strategies.

Rio de Janeiro

April, 2018

Agradecimentos

Gostaria de agradecer à minha avó Augusta, à minha irmã Mariana, ao meu padrinho Júnior e às famílias Torres e Machado pelo apoio, amor e carinho de sempre. Em especial, à pessoa que mais acreditou em mim e cujos ensinamentos de vida eu trago sempre comigo: minha querida mãe. Agradeço também ao meu pai, por tudo que ele me ensinou e me proporcionou, principalmente com relação à construção da minha carreira. Ao meu irmão Kaio e à minha madrasta e amiga Keilla, por todas as risadas nos momentos felizes e abraços nos que precisei. À minha avó Luzia, ao meu avô Vicente e a toda a família Garcia.

Obrigada ao meu querido companheiro, por ter sido meu anjo da guarda, meu porto seguro e por ter caminhado junto a mim nos últimos anos. Obrigada por me ajudar a construir o meu caminho, a alcançar os meus sonhos e a buscar a melhor versão de mim.

Ademais, sou extremamente grata por ter tido contato com pessoas maravilhosas desde que decidi mudar o rumo da minha carreira. Meu orientador Miguel Quartin me deu coragem para enfrentar essa mudança tão grande na minha vida. Ele me apoiou e acreditou em mim desde o início, e por isso serei eternamente grata. Minha coorientadora Beatriz Siffert e minha mentora Karín Menéndez-Delmestre foram dois anjos que entraram na minha vida; sou grata por sua ajuda nos momentos mais difíceis dos dois últimos anos e por terem compartilhado comigo a felicidade das minhas conquistas. Também sou grata aos meus amigos Lucas, Xiaohao, Marcelo, William e Rodrigo, e aos meus colegas do Instituto de Física da UFRJ e do Observatório do Valongo, pelo intercâmbio de conhecimento e de risadas na minha rotina, e aos professores Thiago Gonçalves, Ribamar

Reis, Maurício Calvão, Armando Bernui, Gustavo Mello e Wagner Marcolino, por grande parte do conhecimento que adquiri no mestrado.

Agradeço ao Brasil e à CAPES, pelo financiamento; ao Observatório do Valongo e ao Instituto de Física da UFRJ, por terem me acolhido nos últimos anos; ao ARCOS e ao LASEX, dois grupos dos quais eu me orgulho de ter feito parte; e à banca da defesa dessa dissertação, pela dedicação na leitura e pelas sugestões proporcionadas.

Contents

List of Figures

List of Tables

Chapter 1

Introduction

Two decades ago, Type Ia supernovae, the only established high-redshift standard candles, revealed the presence of the dark energy, which is opposing the attractive force of gravity and is instead accelerating the Universe's rate of expansion (Hamuy et al. (1996); Perlmutter et al. (1998); Riess et al. (1998)). Because of their high luminosity and standardizable light curves, Type Ia supernovae help determine the properties of the dark energy component and constrain cosmological parameters. They then represent a driving area in Cosmology, which aims to expand our knowledge of the Universe.

Many supernova (SN) surveys - including the Dark Energy Survey (DES - Abbott et al. (2016)), the Large Synoptic Survey Telescope (LSST - Abell (2009)), and the Zwicky Transient Facility (ZTF - Bellm (2014)) - are being conducted or planned in the next years, which will increase the number of observed explosions from the current $\sim 10^3$ (Betoule et al. (2014), Scolnic (2018)) to over $\sim 10^6$ (Abell 2009) and, consequently, increase the confidence level related to the cosmological parameters estimation. However, the systematic errors are already of the same order of magnitude as the statistical ones (Davis et al. 2011). This means that although telescope specifications and survey strategies are constantly getting better, it is also important to improve our understanding of these errors and correct for the systematics.

One of the ways of turning noise into signal is by using supernova peculiar velocities (PV), which introduce correlations in the supernova magnitudes (Gordon et al. 2007).

This effect was well developed by Hui & Greene (2006) and Davis et al. (2011). The supernova peculiar velocities are often just modeled as Gaussian random terms, and plotted in the supernova Hubble diagram (that relates distance modulus with redshift) considering that its total redshift is due to the expansion of the Universe. Figure (1.1) shows the Hubble diagram for 472 Type Ia supernovae from the Sloan Digital Sky Survey (SDSS, Holtzman et al. (2008), Kessler et al. (2009a)), the Supernova Legacy Survey (SNLS, Astier et al. (2006), Sullivan et al. (2011)) and the Hubble Space Telescope [survey] (HST, Riess et al. (1998)) plus a nearby supernova set built with the combination of five samples: Calán/Tololo (Hamuy et al. 1996), CfAI (Riess et al. 1998), CfAII (Jha et al. 2007), CfAIII (Hicken et al. 2009) and CSP (Contreras et al. 2010).

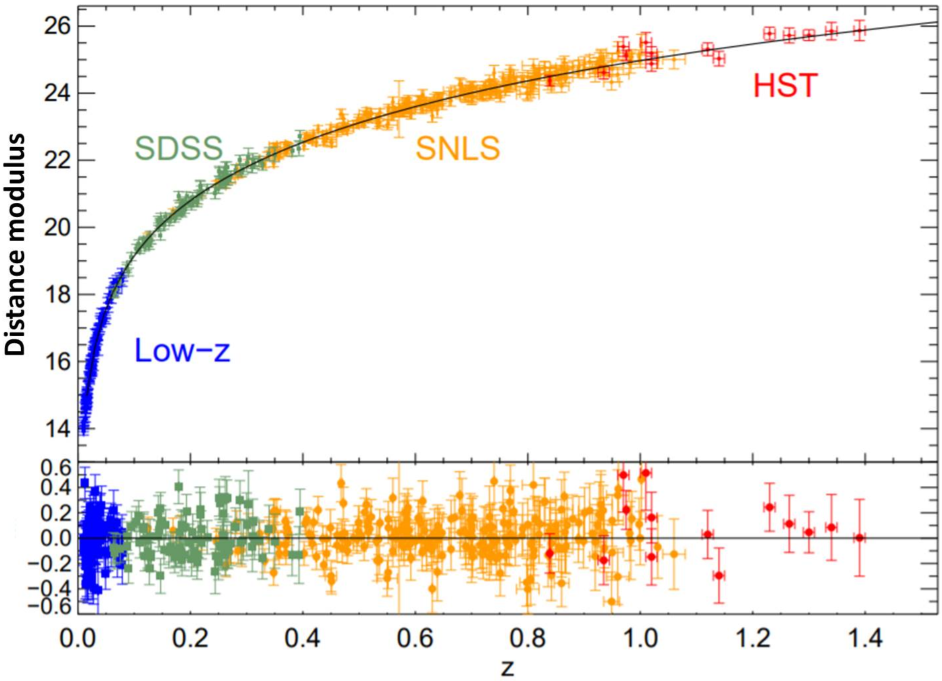

Figure 1.1: Hubble diagram for 472 Type Ia supernovae (123 low-z, 93 SDSS, 242 SNLS, 14 HST), with the residuals from the best fit shown in the bottom panel. Credits: Conley (2011)

Meanwhile, supernova velocities are not really random, as the large-scale gravitational potential wells incur in coherent velocity flows. Any two supernovae in the same region of the sky (which extends to many dozen of Mpc) are supposed to have correlated magnitude fluctuations. In other words, if a given supernova is dimmer than the average because it is moving away from us, a nearby supernova has an excess probability of also being dimmer than the average because it will be in the same velocity flow. The amplitude of these correlations depends on cosmology, as they are directly related to the 2-point correlation function of matter and, therefore, to the matter power spectrum. Consequently, one can obtain the amplitude of the matter fluctuations from the correlation between peculiar velocities. At the scale of 8 Mpc/h, this amplitude is called σ_8, expressing how overdense are the 8 Mpc/h structures in the Universe. Besides that, with the peculiar velocity fields we are also able to constrain the value of the growth rate index γ (related to the common parametrization for the linear growth rate of structure), considered a fixed parameter in ΛCDM.

This project aims to optimize survey strategies in order to measure peculiar velocity fields with Type Ia supernovae. By varying observational parameters, such as the area of the sky, the depth being reached, and the duration of the survey, we studied what strategies could give us the best estimation on σ_8 and γ, via peculiar velocity studies. This kind of analysis is crucial because the deeper we look in the sky, the more supernovae we see (which improves our sample, until a certain redshift determined by the telescope capabilities, of course), but also the larger is the contribution of the cosmological redshift, and the harder is to distinguish the contribution of the peculiar velocity fields. So, depth and field area must be well balanced to optimize observations.

We are currently performing simulations based on DES, LSST and ZTF specifications and strategies to make comparisons on how well they will constrain σ_8 and γ. DES will use only a small fraction of the survey time to observe small patches of sky (30 deg^2) once a week to discover transients, while LSST and ZTF will cover a huge area of the sky (at least 18.000 deg^2) with a frequency that enables images of every part of the visible sky to be obtained every few nights. Results for this analysis will be presented in an upcoming paper: Garcia et al. (2018).

This dissertation is organized as follows: Chapter 2 introduces some cosmology concepts necessary for the understanding of the next chapters; Chapter 3 gives an overview about supernova cosmology and shows how we use supernova peculiar velocities to constrain perturbation parameters; Chapter 4 explains how we performed the simulations and made the comparison among survey strategies; and Chapter 5 presents conclusions and future works.

Chapter 2

Cosmology Concepts

2.1 Standard Model of Cosmology

The standard model of cosmology is the Lambda Cold Dark Matter model (ΛCDM), which can be described as an homogeneous and isotropic universe, that expanded from a hot and dense state and whose dynamics was dominated by different components during its evolution. It is based on the general relativity and the cosmological principle, supporting that the universe looks the same (on average) for an observer at rest, wherever he is. It is also the simplest model that reasonably explains the existence and structure of the Cosmic Microwave Background (CMB), the large-scale structure in the distribution of galaxies and clusters, the abundances of hydrogen, helium and lithium, and the accelerating expansion of the universe.

The letter 'Λ' represents the cosmological constant, which in ΛCDM is associated with the dark energy used to explain the current accelerating expansion of space against the attractive effects of gravity. The cosmological constant has negative pressure, which contributes to the stress-energy tensor that causes accelerating expansion, according to the general theory of relativity. The term 'Dark Matter' is postulated in order to account for gravitational effects observed in large-scale structures that cannot be accounted for by the quantity of observed matter; and 'Cold' means that dark matter's velocity was far less than the speed of light at the epoch of radiation-matter equality.

The most general metric to describe an expanding universe that obeys the cosmological principle is the Friedmann-Lemaitre-Robertson-Walker (FLRW) metric

$$ds^2 = -c^2dt^2 + a(t)^2 \left[\frac{dr^2}{1-\kappa r^2} + r^2(d\theta^2 + sin^2\theta d\phi^2) \right], \tag{2.1}$$

where r, ϕ and θ are comoving coordinates, t is time (counted from the birth of the universe), $a(t)$ is the scale factor and κ is the curvature parameter, which can assume the values -1 (negative curvature), 0 (plane) and +1 (positive curvature).

The scale factor $a(t)$ is a parametrization to the expansion of the universe (defined relative to the present day), and is related to the observed redshift z of an object whose light was emitted at time t_{em} by

$$\frac{1}{a(t_{em})} = 1 + z. \tag{2.2}$$

We use the time-derivative of the scale factor ($\dot{a}$) divided by the scale factor itself to give the time-dependent Hubble parameter (that represents the expansion rate of the Universe)

$$H(t) = \frac{\dot{a}}{a}. \tag{2.3}$$

By combining the Einstein's field equations and the FLRW metric, and supposing that the universe components behave as perfect fluids, we have two independent equations that give the expansion rate in terms of the matter+radiation density ρ, the curvature κ, the cosmological constant Λ, the gravitational constant G, and the pressure of the fluid p:

$$H^2 = \left(\frac{\dot{a}}{a}\right)^2 = \frac{8\pi G}{3}\rho - \frac{\kappa}{a^2} + \frac{\Lambda}{3}, \tag{2.4}$$

and

$$\frac{\ddot{a}}{a} = -\frac{4\pi G}{3}(\rho + 3p) + \frac{\Lambda}{3}. \tag{2.5}$$

We can interpret the cosmological constant as one of the components of the Universe with density $\rho_\Lambda \equiv \Lambda/8\pi G$ and pressure $p_\Lambda \equiv -\Lambda/8\pi G$. So we can simplify the above equations and get to the Friedmann ones:

$$H^2 = \left(\frac{\dot{a}}{a}\right)^2 = \frac{8\pi G}{3}\rho - \frac{\kappa}{a^2}, \tag{2.6}$$

and

$$\frac{\ddot{a}}{a} = -\frac{4\pi G}{3}(\rho + 3p), \tag{2.7}$$

that combined give the third dynamics equation, the fluid equation

$$\dot{\rho} + 3\frac{\dot{a}}{a}(\rho + p) = 0. \tag{2.8}$$

Eq. (2.6) and (2.7) give us two independent equations but three variables, making it impossible to find a solution for this system. One way of moving forward with this analysis is by using an equation of state, to relate pressure and energy density. Since the density of the components of the Universe is currently low, linear equations of state provide a good approximation, where $p_i = w_i\rho_i$, w_i is the equation of state parameter and the index i represents the different components. If we combine the equation of state with the fluid Eq. (2.8), we have

$$\dot{\rho}_i + 3\frac{\dot{a}}{a}(1 + w_i)\rho_i = 0, \tag{2.9}$$

which is the same as

$$\frac{\dot{\rho}_i}{\rho_i} = -3\frac{\dot{a}}{a}(1 + w_i). \tag{2.10}$$

By integrating and rearranging the last equation, we get to the equation that governs the evolution of the different components in terms of the scale factor:

$$\rho_i(a) = \rho_{i,0}a^{-3(1+w_i)}. \tag{2.11}$$

The flat ΛCDM model considers three components: radiation ($w_{rad} = 1/3$), matter ($w_m = 0$) and dark energy ($w_\Lambda = -1$). A useful way to study the Friedmann equations is by defining the density parameter for each of these components as

$$\Omega_i = \frac{\rho_i}{\rho_{crit}}, \tag{2.12}$$

where $\rho_{crit} = 3c^2H^2/3\pi G$ is the critical energy density (the one a perfectly flat Universe would have).

The different energy densities decay modes for each component of the universe lead it through different eras, each one dominated by one of these fluids. One can see the different eras in Figure (2.1).

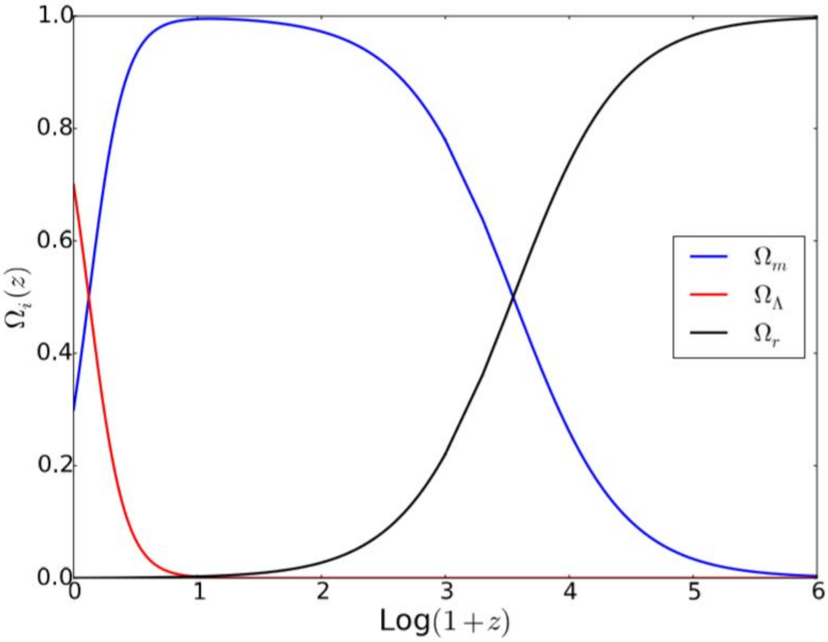

Figure 2.1: Density parameter values for the different components of the universe as a function of the redshift. Credits: Sánchez (2018)

Based on the various density parameters (which add up to 1), the Friedmann equation can be rewritten as

$$H(a) \equiv \frac{\dot{a}}{a} = H_0 E(a), \tag{2.13}$$

with

$$E(a) = \sqrt{(\Omega_c + \Omega_b)a^{-3} + \Omega_r a^{-4} + \Omega_\kappa a^{-2} + \Omega_\Lambda a^{-3(1+w)}}, \tag{2.14}$$

where w is the equation of state for dark energy assuming negligible neutrino mass, Ω_c is the dark matter density parameter, Ω_b is the baryon density parameter, Ω_r is the radiation density parameter, Ω_κ represents the curvature of the Universe, and Ω_Λ is the dark energy density parameter.

The ΛCDM model is based on six parameters: Ω_b, Ω_c, the Hubble parameter (H_0); the scalar spectral index (n_s); the curvature fluctuation amplitude; and the reionization optical depth (τ). Commonly, the set of observations used to fit cosmological parameters includes the CMB anisotropy, the brightness/redshift relation for supernovae, large-scale galaxy clustering (including the baryon acoustic oscillation feature, or BAO), weak gravitational lensing and globular cluster ages.

If curvature Ω_κ is assumed zero and the equation of state for dark energy w is -1, the Friedmann equation simplifies to

$$H(a) = H_0\sqrt{\Omega_m a^{-3} + \Omega_r a^{-4} + \Omega_\Lambda}. \tag{2.15}$$

The definitions and explanations about the ΛCDM model presented in this section were based on Ryden (2003) and Coles & Lucchin (2002), which can be revised for more details.

The results based on full-mission Planck observations of temperature and polarization anisotropies of the CMB are consistent with the six-parameter ΛCDM cosmology (Planck Collaboration 2016). Planck found a Hubble constant $H_0 = (67.8 \pm 0.9)$ km/s/Mpc, a matter density parameter $\Omega_m = 0.308 \pm 0.012$, and a scalar spectral index with $n_s = 0.968 \pm 0.006$. Combined with Planck temperature and lensing data, Planck Low Frequency Instrument (LFI) polarization measurements lead to a reionization optical depth $\tau = 0.066 \pm 0.016$. Spatial curvature is found to be $|\Omega_\kappa| < 0.005$ and the equation of state of dark energy is constrained to $w = -1.006 \pm 0.045$.

Planck results are in agreement with Baryonic Acustic Oscilations (BAO) data (Beutler et al. (2011); Anderson et al. (2014); Ross et al. (2015)) and with the Joint Light-curve Analysis (JLA) supernovae sample (Betoule et al. 2014). However, the amplitude of the fluctuations is found to be higher than inferred from rich cluster counts and weak gravitational lensing. Moreover, the currently most precise measurement of H_0 (Riess et al. 2016) differs by ~ 3.4 standard deviations from the value reported by Planck Collaboration (2016). Apart from these tensions, the base ΛCDM cosmology provides an excellent description of the Planck CMB observations and many other astrophysical data sets.

2.2 Dark Energy Models

Although ΛCDM is the current benchmark cosmological model, alternative models for dark energy are extensively studied in the literature. There are a lot of different approaches trying to describe the dark energy, like the inclusion of new fields with different couplings to geometry quantities or the parametrization of the dark energy equation of state. Anyway, the dark energy models can be tested by analyzing its effect over the expansion rate of the Universe (via $H(z)$). The particular form of the Hubble parameter depends on the model, but considering that all components are conserved independently, the expansion parameter is described as

$$H^2(z) = H_0^2[\Omega_r(1+z)^4 + \Omega_m(1+z)^3 + \Omega_\kappa(1+z)^2 + \Omega_x f(z)], \tag{2.16}$$

where Ω_x is the current fraction of the energy density related to the dark energy, and $f(z)$ is its evolution function given by

$$f(z) \equiv \frac{\rho(z)}{\rho_0} = \exp\left(3\int_0^z \frac{1+w(z')}{1+z'}dz'\right). \tag{2.17}$$

Regardless of the mechanism used (inclusion of new fields or a parametrization), the equation of state $w(z)$ determines the evolution of the dark energy.

Table (2.1) presents recent values for the cosmological parameters obtained by combining different observables to varying models describing the dark energy. Constraints were based on Galaxy+Lyman-alpha Forest (LyaF) BAO data, the combination of Planck temperature and Wilkinson Microwave Anisotropy Probe (WMAP) polarization measurements of the CMB fluctuation (Planck+WP), the Nine-Year WMAP (WMAP9), and the Joint Light-curve Analysis (JLA) supernova data. The dark energy is represented by the cosmological constant Λ, by a fluid with equation of state $w(z) = w$, or by a fluid with equation of state $w = w_0 + (1-a)w_a$. Figures (3.3) and (3.4) in the next chapter show the constraints on the most representative parameters of those three models.

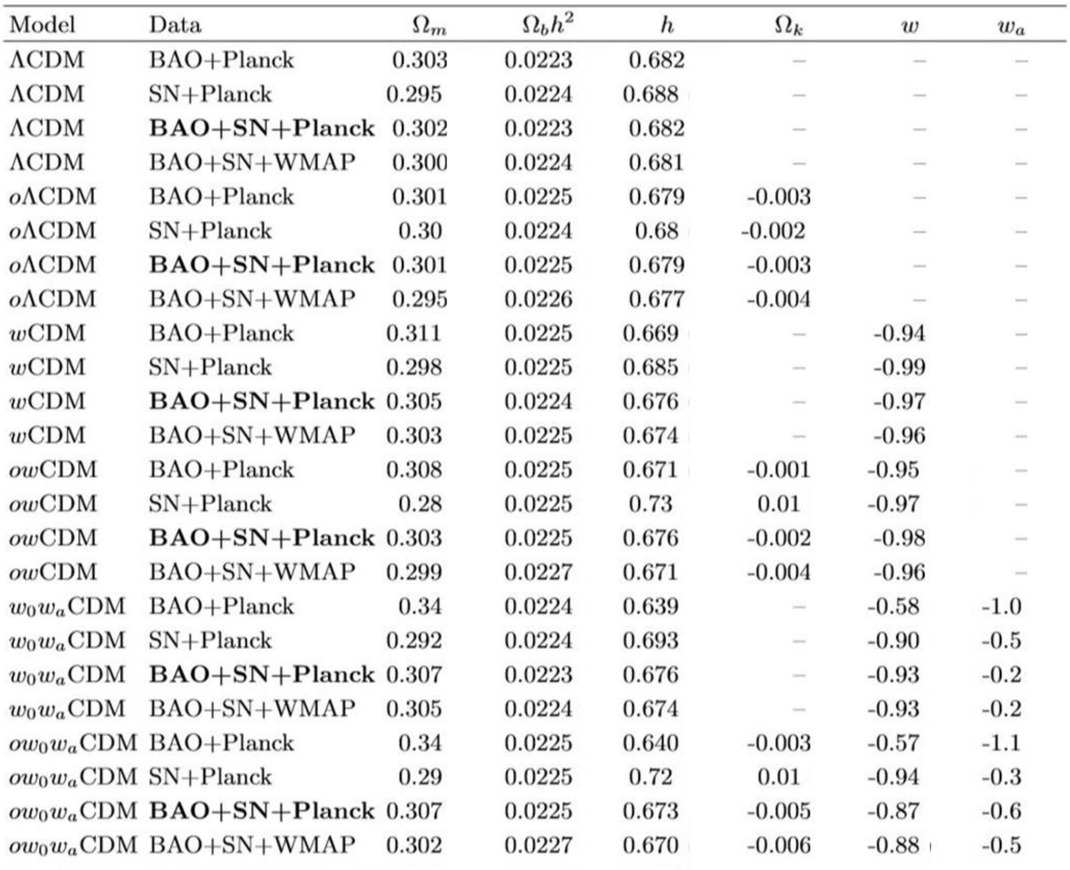

Model	Data	Ω_m	$\Omega_b h^2$	h	Ω_k	w	w_a
ΛCDM	BAO+Planck	0.303	0.0223	0.682	–	–	–
ΛCDM	SN+Planck	0.295	0.0224	0.688	–	–	–
ΛCDM	**BAO+SN+Planck**	0.302	0.0223	0.682	–	–	–
ΛCDM	BAO+SN+WMAP	0.300	0.0224	0.681	–	–	–
oΛCDM	BAO+Planck	0.301	0.0225	0.679	-0.003	–	–
oΛCDM	SN+Planck	0.30	0.0224	0.68	-0.002	–	–
oΛCDM	**BAO+SN+Planck**	0.301	0.0225	0.679	-0.003	–	–
oΛCDM	BAO+SN+WMAP	0.295	0.0226	0.677	-0.004	–	–
wCDM	BAO+Planck	0.311	0.0225	0.669	–	-0.94	–
wCDM	SN+Planck	0.298	0.0225	0.685	–	-0.99	–
wCDM	**BAO+SN+Planck**	0.305	0.0224	0.676	–	-0.97	–
wCDM	BAO+SN+WMAP	0.303	0.0225	0.674	–	-0.96	–
owCDM	BAO+Planck	0.308	0.0225	0.671	-0.001	-0.95	–
owCDM	SN+Planck	0.28	0.0225	0.73	0.01	-0.97	–
owCDM	**BAO+SN+Planck**	0.303	0.0225	0.676	-0.002	-0.98	–
owCDM	BAO+SN+WMAP	0.299	0.0227	0.671	-0.004	-0.96	–
w_0w_aCDM	BAO+Planck	0.34	0.0224	0.639	–	-0.58	-1.0
w_0w_aCDM	SN+Planck	0.292	0.0224	0.693	–	-0.90	-0.5
w_0w_aCDM	**BAO+SN+Planck**	0.307	0.0223	0.676	–	-0.93	-0.2
w_0w_aCDM	BAO+SN+WMAP	0.305	0.0224	0.674	–	-0.93	-0.2
ow_0w_aCDM	BAO+Planck	0.34	0.0225	0.640	-0.003	-0.57	-1.1
ow_0w_aCDM	SN+Planck	0.29	0.0225	0.72	0.01	-0.94	-0.3
ow_0w_aCDM	**BAO+SN+Planck**	0.307	0.0225	0.673	-0.005	-0.87	-0.6
ow_0w_aCDM	BAO+SN+WMAP	0.302	0.0227	0.670	-0.006	-0.88	-0.5

Table 2.1: Cosmological parameter constraints from Galaxy+LyaF BAO data combined with a compressed description of CMB constraints from Planck+WP or WMAP9, and the JLA SN data. Entries for which the parameter is fixed in the listed cosmological model are marked with a dash. For w_0w_aCDM and ow_0w_aCDM, column 7 lists the value of w at $z = 0.266$, which is the "pivot" redshift for w_0w_aCDM with the full data combination. Credits: Aubourg et al. (2014).

2.3 Distances in Cosmology

The concept of simultaneity was totally reformulated by Special Relativity. The definition we once had about distance, as being absolute and unequivocal, was deeply affected by this theory; and we discovered that in fact the definition of distance depends on the motivation.

Within the Solar System, for example, we measure the distance to the Moon and planets by reflecting radar signals from them. For the purpose of determining distances to stars within the Milky Way galaxy, the most used method is the trigonometric parallax. Although this method is not suited to measure distances to high-redshift objects, it is used to calibrate other measurement methods.

When dealing with much more distant objects, we enter the realm of cosmological distances. There are different definitions of such distances, and we integrate the Eq. (2.15) in order to get them. They all coincide for sufficiently small redshifts, but differ in their fundamental concept and usage. In the following sections, I present the most used definitions, that can be revised in more detail in Hogg (2000).

On cosmological scales, there are two known methods to measure distances. One is by using objects with a known brightness, called the standard candle method, and the other method is by using an object with known size, called the standard ruler method.

2.3.1 Proper Distance and Comoving Distance

Proper distance and comoving distance are closely related distance measures. The main difference is that proper distance changes over time due to the expansion of the Universe while the comoving distance does not.

If we are observing an object moving with the Hubble flow, i.e. moving due solely to the expansion of the Universe, its proper distance is defined as

$$D_P(t) = a(t) \int_0^r \frac{dr'}{\sqrt{1-\kappa(\frac{r'}{R_0})^2}} = a(t)\chi(r), \tag{2.18}$$

where

$$\chi(r) = \begin{cases} R_0 \sin^{-1} r/R_0 : \kappa = +1 \\ r : \kappa = 0 \\ R_0 \sinh^{-1} r/R_0 : \kappa = -1 \end{cases}, \tag{2.19}$$

and R_0 is the intrinsic curvature of space.

The comoving distance $\delta\chi$ between two nearby objects moving with the Hubble flow is the distance that remains constant with epoch. This is the proper distance multiplied by $(1+z)$. So the line-of-sight comoving distance χ from us to a distant object is the integration of the $\delta\chi$ contributions between nearby events along the radial ray from $z=0$ to the object, i.e.:

$$\chi = D_H \int \frac{dz'}{E(z')}, \tag{2.20}$$

where $D_H \equiv c/H_0$ is the Hubble distance and $E(z) \equiv \sqrt{\Omega_M(1+z)^3 + \Omega_\kappa(1+z)^2 + \Omega_\Lambda}$.

The comoving distance of two objects at the same redshift separated by an angle $\delta\theta$ is $D_M\delta\theta$, where D_M is called the transverse comoving distance

$$D_M = D_H \frac{1}{\sqrt{\Omega_\kappa}} \sinh(\sqrt{\Omega_\kappa}\chi/D_H). \tag{2.21}$$

In order to measure comoving distances we use the radial BAO: frozen relics left over from the pre-decoupling universe, after which baryons and photons started evolving independently (z = 1090), and whose characteristic scale known as the sound horizon scale has been precisely measured by CMB probes.

2.3.2 Luminosity Distance

The luminosity distance D_L is defined by the relationship between bolometric flux f (the integral over all frequencies of the spectral flux) and bolometric luminosity L (the integral over all frequencies of the spectral luminosity):

$$D_L \equiv \left(\frac{L}{4\pi f}\right)^{1/2}. \tag{2.22}$$

In an expanding, spatially curved universe, the relation between the observed flux f and the luminosity L of a distant light source is

$$f = \left(\frac{L}{4\pi\chi(r)^2(1+z)^2}\right), \tag{2.23}$$

and the luminosity distance D_L is

$$D_L = \chi(r)(1+z). \tag{2.24}$$

For a flat Universe, we have:

$$D_L = r(1+z) = \chi(1+z), \tag{2.25}$$

where t_0 is the time in the observer's rest frame.

There is a convenient way of relating the distance to an astronomical object to its bolometric magnitudes, through the quantity called distance modulus:

$$\mu := m - M, \tag{2.26}$$

which is the magnitude difference between the object's bolometric flux and the flux it would have if it was 10 pc away from the observer (in the observer's reference frame):

$$\mu \equiv 5\log_{10}\left(\frac{D_L}{10pc}\right). \tag{2.27}$$

The apparent magnitude is the sum of the absolute magnitude of the object, the distance modulus and the K-correction. K-correction is an adjustment made to an astronomical object's magnitude (or flux) that allows a measurement of a quantity of light emitted at a redshift z to be converted to an equivalent measurement in the rest frame of the object. It is needed because an astronomical measurement through a single filter or a single bandpass only sees a fraction of the total spectrum, redshifted into the frame of the observer. In order to compare the measurements through a filter of objects at different redshifts, one needs to make this correction.

To take into account the absolute magnitude, one needs a standard candle (an object of known absolute magnitude), making it possible to calculate its luminosity distance. The most commonly used standard candles in astronomy are Cepheid Variables (since their absolute magnitude can be determined from their variability period), and Type Ia supernovae (since their peak luminosity is correlated with how quickly their light curve declines after maximum light). In chapter 3, I make an overview about Type Ia supernovae and how we do cosmology with them.

Another way of measuring luminosity distances is by using gravitational waves, which provide a direct measure of the distance, but give no independent information about redshift, so an electromagnetic counterpart is needed (Zhao et al. (2011); Taylor & Gair (2012)).

2.3.3 Angular-Diameter Distance

Another distance measure that can be computed using the observable properties of cosmological objects is the angular-diameter distance. By observing an object whose proper length is known (a standard ruler) and measuring its angular size, one can make estimations on cosmological parameters because the relation between these two distances depends on the assumed cosmological model.

Consider a standard ruler of constant proper length l, aligned perpendicular to the line of sight, with angular size θ between its edges, at redshift z. If θ is very small, the angular-distance to the standard ruler is given by

$$D_A \equiv \frac{l}{\theta} = \frac{\chi(r)}{1+z}. \tag{2.28}$$

Comparing with the proper distance and the luminosity distance formulas, one can find that

$$D_A = \frac{D_P(t_0)}{1+z} = \frac{D_L}{(1+z)^2}. \tag{2.29}$$

There are two ways of measuring the angular-diameter distance: using the angular BAO or gravitational lensing. Since BAO is a generic result of interactions between photons and baryons, the BAO feature exists not only in the CMB, but also in the matter distribution. As collapsed objects growing inside over dense regions, galaxies can be used as tracers of matter distribution by assuming some appropriate galaxy bias. This way, BAO matter clustering provides a standard ruler for length scale in cosmology, but it requires substantial resources and many years of dedicated observations. Another way of measuring D_A is by using gravitational lensing. The angular diameter distance to the lens can be determined by measuring both the time delay between two spatially separated images of a single source via strong lensing, and the velocity dispersion of the lensed galaxy.

2.4 Large Scale Structure

The Large Scale Structure of the Universe refers to the patterns of galaxies and matter on scales much larger than individual galaxies or groupings of galaxies. On large scales, the Universe displays a coherent structure, with galaxies residing in groups and clusters on scales of $\sim 1-3$ h^{-1} Mpc, which lie at the intersections of long filaments of galaxies that are > 10 h^{-1} Mpc in length. Vast regions of relatively empty space (the voids) contain very few galaxies and span the volume in between these structures (Coil 2012). Figure (2.2) shows the spatial distribution of galaxies as a function of redshift from the 2-degree Field (2dF) Galaxy Redshift Survey. The observed large scale structure depends both on cosmological parameters and the formation and evolution of galaxies.

In order to quantify the clustering of galaxies, one must survey the entire galaxy density distribution, from voids to superclusters. Any galaxy survey will observe a radial distribution of galaxies and need to correct for a spatially varying galaxy selection function (Percival 2013). So we use the expected mean density of the universe $\bar{\rho}(x)$ to translate the observed galaxy density $\rho(x)$ to a dimensionless over-density

$$\delta(x) = \frac{\rho(x) - \bar{\rho}(x)}{\bar{\rho}(x)}, \tag{2.30}$$

which has a distribution that is close to that of a Gaussian, adiabatic fluctuations for large scales. So the statistical distribution is described by the 2-point functions of this field.

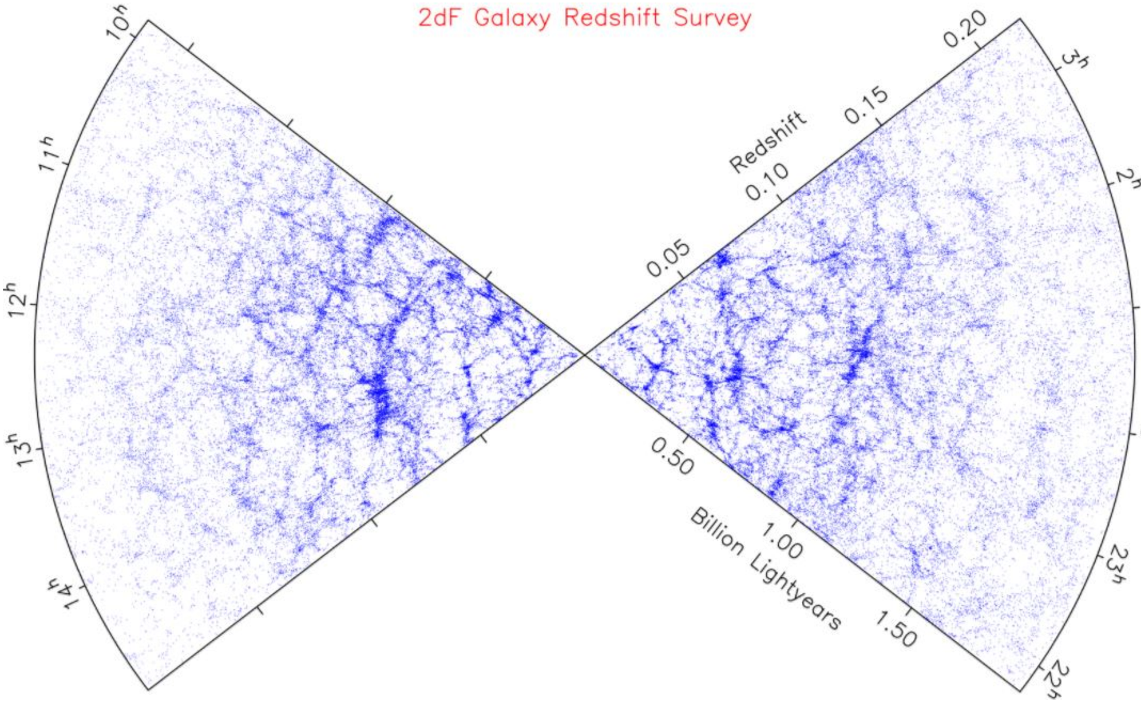

Figure 2.2: The spatial distribution of galaxies as a function of redshift and right ascension (projected through 3 degrees in declination) from the 2dF Galaxy Redshift Survey. Credits: Colless et al. (2003).

A commonly used quantitative measure of large scale structure is the galaxy 2-point correlation function, $\xi(x)$, which is the expected 2-point function of this statistic and traces the amplitude of galaxy clustering as a function of scale

$$\xi(x1, x2) \equiv \langle \delta(x1)\delta(x2) \rangle, \tag{2.31}$$

where $x1$ and $x2$ are the vectors pointing toward supernovae i and j, respectively. Considering homogeneity and isotropy, we have that

$$\xi(x1, x2) = \xi(x1 - x2) = \xi(\mid x1 - x2 \mid). \tag{2.32}$$

Using the mean number of galaxies per unit volume $\bar{n}$ and two small regions δV_1 and δV_2, separated by a distance r, we can calculate the expected number of pairs of galaxies with one galaxy in δV_1 and the other in δV_2

$$\langle n_{pair} \rangle = \bar{n}^2[1 + \xi(r)]\delta V_1 \delta V_2. \tag{2.33}$$

If $\xi(r) = 0$, the galaxies are uncorrelated (randomly distributed) on this scale. $\xi(r) > 0$ corresponds to clustering, and $\xi(r) < 0$ to anti-clustering.

It is often convenient to measure clustering in Fourier space. The Fourier transform of the 2-point correlation function is the power spectrum, which is often used to describe the distribution of galaxies and clusters of galaxies, and is defined as

$$P(k1, k2) = \frac{1}{(2\pi)^3} \langle \delta(k1)\delta(k2) \rangle, \tag{2.34}$$

where k1 and k2 represent the possible wavenumbers. The statistical homogeneity and isotropy gives

$$P(k1, k2) = \delta_D(k1 - k2)P(k1), \tag{2.35}$$

where δ_D is the Dirac delta function. The correlation function and power spectrum form the following Fourier pair:

$$P(k) = \int \xi(r) e^{ikx} d^3x, \tag{2.36}$$

$$\xi(x) = \int P(k) e^{-ikx} \frac{d^3k}{(2\pi)^3}. \tag{2.37}$$

Measuring either the correlation function or the power spectrum provides a statistically complete description of the Gaussian field. The present-day matter power spectrum is the evolved result of the primordial power spectrum produced during inflation, a period of rapid acceleration in the early Universe.

It is possible to calculate the mean quadratic value of the matter contrast, which indicates where there are local enhancements in matter density, as a function of the power spectrum:

$$\sigma_R^2(t) = \frac{V}{(2\pi)^3} \int P(k) \mid f(kR) \mid^2 d^3k, \tag{2.38}$$

where $f(kR)$ is the Fourier transform of the window function. In order to compare theory with observations, we can take also the purely statistics formula:

$$\sigma_R^2(t) = \left\langle \left(\frac{1}{V} \int_V \delta(x, t) d^3x \right)^2 \right\rangle, \tag{2.39}$$

where V is the comoving volume of the sample and the average is about different universe samples with volume $V = 4\pi R^3/3a_0^3$. This kind of analysis is traditionally done with clusters of galaxies, which have characteristic dimensions of the order of 8 Mpc/h. From that, we define σ_8: the amplitude of the matter fluctuations at the scale of 8 Mpc/h,

$$\sigma_8 \equiv \sqrt{\int dk \frac{k^2}{2\pi^2} \frac{9P(k)}{(kR)^6} \left[\sin(kR) - kR\cos(kR)\right]^2}, \tag{2.40}$$

where $R \equiv 8\text{Mpc/h}$. σ_8 represents a measure of the Universe's inhomogeneity by expressing how overdense the 8 Mpc/h structures are.

Another useful parameter to describe large scale structure evolution is γ, the growth rate index related to the common parametrization for the linear growth rate f (Lahav et al. 1991):

$$f(a) = -\frac{d\ln G(a)}{d\ln a} \simeq \Omega_m(a)^\gamma, \tag{2.41}$$

where $G(a)$ is the growth function:

$$G(a) = \frac{5\Omega_m(a)}{2H_0^3} \int_0^a \frac{da'}{(a'E(a'))^3}, \tag{2.42}$$

and

$$\Omega_m(a) = \frac{\Omega_{m,0}}{a^3 E^2(a)}. \tag{2.43}$$

Within General Relativity and for the ΛCDM model, $\gamma = \gamma_{\Lambda CDM} \approx 0.55$. Since γ does not depend strongly on the equation of state parameter of dark energy, it is often employed as a simple way of describing the growth rate in modified gravity models.

Chapter 3

Type Ia Supernovae and Peculiar Velocity Fields

3.1 Supernova Classification

Supernovae are transient astronomical events that occur during the last stellar evolutionary stages of some stars. This dramatic and catastrophic destruction is marked by one final explosion due to the instability generated by the action of the photodisintegration or neutron degeneracy in their interior, or because of the accretion of matter from one of the stars in a particular binary system. These processes release kinetic and luminous energy and occur once in every 50 years in a typical galaxy.

Supernovae are divided into subclasses, classified according to their light curves and the absorption lines of different chemical elements that appear in their spectra. The first classification criterion is the presence or absence of a hydrogen line. If a supernova's spectrum contains these lines (the Balmer series), it is classified as Type II; otherwise, it is Type I. In each of these two types there are subdivisions according to the presence of lines from elements other than hydrogen or to the shape of the light curve. Type Ia supernovae show a strong ionised silicon absorption line, while Type Ib and Ic have weak or no silicon absorption feature. Type II-P and Type II-L supernovae have no narrow lines, while Type IIn show some narrow lines, and Type IIb have the characteristic that their spectrum changes to become like Type Ib in their late stages.

Supernovae are also classified in Thermonuclear or Core Collapse. Type Ib, Ic and II represent massive stars that undergo core collapse in the end of their lives. Type Ia supernovae happen when a white dwarf star accumulates sufficient material from a stellar companion to raise its core temperature enough to ignite carbon fusion, at which point it undergoes runaway nuclear fusion, completely disrupting it. All those classifications can be summarized in Figure (3.1), taken from Coelho et al. (2015), who makes a good review about this topic.

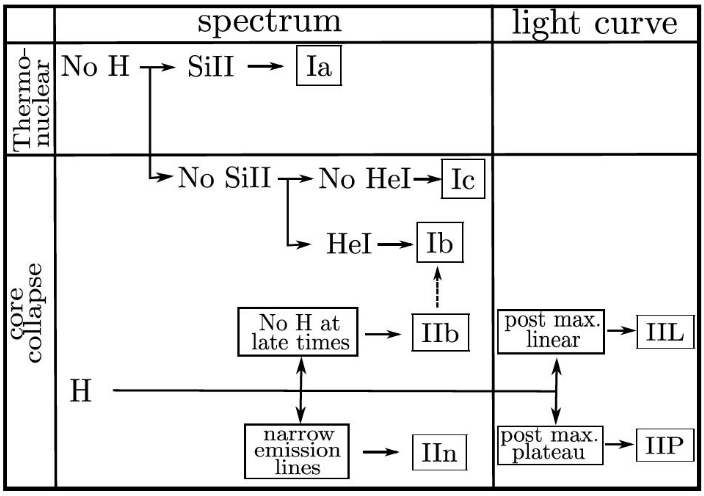

Figure 3.1: Supernovae classification. Credits: Coelho et al. (2015)

3.2 Type Ia Supernovae as Standard Candles

The most interesting supernova subclass to cosmology is the Type Ia supernova. Physically, carbon-oxygen white dwarfs with a low rate of rotation are limited to below 1.44 solar masses (the Chandrasekhar limit mass). If a white dwarf gradually accretes mass from a binary companion, the general hypothesis is that its core will reach the ignition temperature for carbon fusion as it approaches the limit, so the pressure due to the degeneracy of electrons is not suficient to keep the star stable and it collapses. The fact that this class of stars all explode with mass given by the Chandrasekhar limit suggests that all of them should have similar characteristics, and could behave as standard candles. Observations showed that this is not quite true, but the discovery of a correlation between peak luminosity and how quickly the light curve declines after maximum, made it possible to standardize Type Ia supernova, and they can be made into standard candles by correcting for this effect. Figure (3.2) depicts one such procedure, which makes use of the so called stretch parameter. Coelho et al. (2015) reviews this subject by presenting some fundamental concepts related to the cosmological use of Type Ia supernovae, and builds a light curve template to exemplify the procedure.

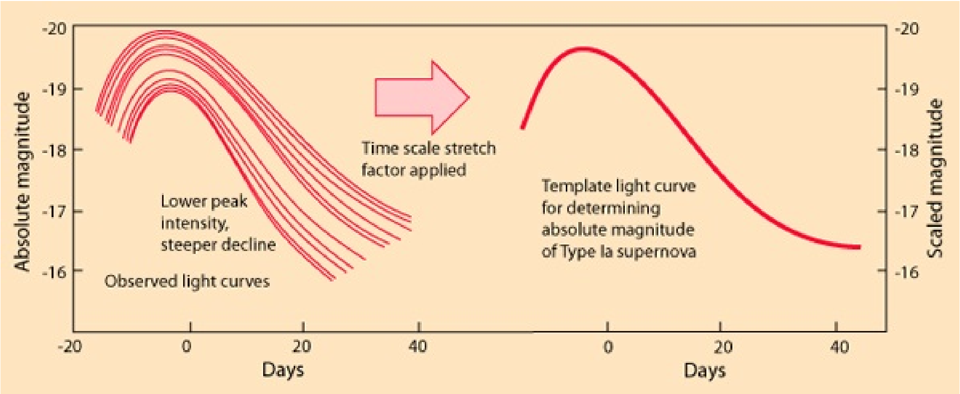

Figure 3.2: Time scale stretch factor application in various supernova light curves in order to determine a standard absolute magnitude. Credits: http://hyperphysics.phy-astr.gsu.edu

There are several light-curve fitters in the literature (Jha et al. (2007); Wang et al. (2003); Guy et al. (2007); Conley (2011)). The most commonly used are the multicolor light-curve shape (MLCS2k2), by Jha et al. (2007), and the spectral adaptive light-curve template (SALT2), by Guy et al. (2007), which are discussed in the following sections based on Lago et al. (2011).

The MLCS2k2 fitting model describes the variation among Type Ia supernova light curves with a single parameter (Δ). The theoretical magnitude, $m^{th}_{Y,\gamma}$, observed in an arbitrary filter Y, at an epoch γ, is given by

$$m^{th}_{Y,\gamma} = M_{Y',\gamma} + p_{Y',\gamma}\Delta + q_{Y',\gamma}\Delta^2 + K_{Y'Y,\gamma} + \mu + X^{host}_{Y',\gamma} + X^{MW}_{Y}, \tag{3.1}$$

where $Y' \in U, B, V, R, I$ is one of the supernova rest-frame filters for which the model is defined, Δ is the MLCS2k2 shape-luminosity parameter that accounts for the correlation between peak luminosity and the shape/duration of the light curve, $X^{host}_{Y',\gamma}$ is the host-galaxy extinction, X^{MW}_{Y} is the Milky Way extinction, $K_{Y'Y,\gamma}$ is the K-correction between rest-frame and observer-frame filters, and μ is the distance modulus. The coefficients $M_{Y',\gamma}$, $p_{Y',\gamma}$ and $q_{Y',\gamma}$ are model vectors that have been evaluated using nearly 100 well observed low-redshift Type Ia supernovae as a training set. Above, $\gamma = 0$ labels quantities at the B-band peak magnitude epoch. Fitting the model to the magnitudes of each Type Ia supernova, usually fixing R_V (the ratio of V band extinction to color excess at B-band peak), gives μ (the distance modulus), Δ, A_V (the V band extinction; $A_V = R_V \times E(B-V)$) and t_0 (the B-band peak magnitude epoch).

On the other hand, SALT2 uses a two-dimensional surface in time and wavelength to describe the temporal evolution of the rest-frame spectral energy distribution (SED) or specific flux for Type Ia supernovae. The original model was trained with 303 Type Ia supernovae from various redshifts. In SALT2, the rest-frame specific flux at wavelength λ and phase p does depend through the parameters x_0, x_1, and c on the particular Type Ia supernova and is modeled by

$$\phi(p, \lambda; x_0, x_1, c) = x_0[M_0(t, \lambda) + x_1 M_1(t, \lambda)] \exp[cC(\lambda)], \tag{3.2}$$

where $M_0(t, \lambda)$, $M_1(t, \lambda)$ are the zeroth and the first moments of the distribution of training sample SEDs. $M_0(t, \lambda)$, $M_1(t, \lambda)$, and $C(\lambda)$ are determined from the training process described in Guy et al. (2007). In order to compare with photometric Type Ia supernovae data, the observer frame flux in passband Y is calculated as

$$F^Y(p) = \int d\lambda'[\lambda'\phi(p, \lambda')T^Y(\lambda')], \tag{3.3}$$

where $T^Y(\lambda')$ defines the transmission curve of the observer frame filter Y, which represents the fraction of energy that passes through the filter Y as a function of wavelength. This needs to be taken into account because the filters are not perfect, in the sense that they do not let all photons pass, no matter what wavelength is being considered. Considering that time intervals dp_S in the source's rest-frame correspond to time intervals in the detector's frame $dp_D = (1+z)dp_S$, and that the photon energies are also related by a factor $(1+z)$, we can rewrite Eq. (3.3) in the observer's rest frame:

$$F^Y(p(1+z)) = (1+z)\int d\lambda'[\lambda'\phi(p,\lambda')T^Y(\lambda'(1+z))]. \tag{3.4}$$

The parameters x_0, x_1, and c can be determined by fitting each Type Ia supernova light curve separately using Eq. (3.2) and (3.4). However, SALT2 fit does not provide an independent distance modulus (μ_B) estimate for each supernova. We use the parameters retrieved from the light-curve fit to estimate it:

$$\mu_B = x_0 - M + \alpha \times x_1 - \beta \times c, \tag{3.5}$$

where α, β and the absolute magnitude M are parameters which are fitted by minimizing the residuals in the Hubble diagram.

From statistical analysis, it is possible to compare the measurement of μ with the theoretical prediction of a given model. Based on that, the Supernova Cosmology Project and the High-z Supernova Search Team obtained the first clear evidences that the Universe is experiencing an accelerated expansion (Hamuy et al. (1996), Perlmutter et al. (1998), Riess et al. (1998)). Adam Riess, Brian Schimidt and Saul Perlmutter were awarded the 2011 Nobel Prize in Physics for this discovery.

3.3 Cosmology with Type Ia Supernovae

Once the stretch-corrected magnitude and redshift are determined, the supernova can be put into the Hubble diagram in order to measure the cosmological parameters. Since the apparent magnitude of a standard candle gives us its distance and the time at which the light was emitted, and the redshift gives the cosmic expansion parameter $a(t)$, a Hubble diagram populated with supernovae at different distances gives us the history of the expansion of the universe. Since the expansion rate is determined by its matter-energy content, it is clear that Type Ia supernovae can tell us about the properties of the contents of the universe, and, in particular, of the dark energy component.

The statistical uncertainties in the Hubble diagram are dominated by the intrinsic supernova peak magnitude dispersion $\sigma_{int} = 0.10 - 0.15$, and the statistical error achieved by near-future surveys will be $\sigma_{stat} = 0.01 - 0.02$. Since many systematic uncertainties are expected to be fully correlated for supernovae at similar redshifts, but uncorrelated otherwise, it is clear that systematic errors of order a few per cent will be important, and, in many cases, already dominant.

The most common Type Ia supernova cosmological analysis is based on the χ^2 function:

$$\chi^2 := X^T \Sigma^{-1} X, \tag{3.6}$$

where $X := (\mu - \mu_{th}(z, \Theta))$, μ is the set of distance moduli derived from the light curve fitting procedure for each supernova event, at redshifts given by z, $\mu_{th}(z, \Theta)$ is the theoretical prediction for them, given in terms of a vector Θ of parameters and Σ is the covariance matrix of the events.

In the following discussion, we present concepts based on the SALT2 light curve fitter as discussed in Lago et al. (2011). SALT2 gives three quantities to be used in the analysis of cosmology: x_1 (a parameter related to the stretch of the light-curve), c (a parameter related to the color of the supernova alongside its redshift z), and $m_B^\star$ (the peak rest-frame magnitude in the B band), given by:

$$m_B^\star := -2.5 \log[x_0 \int d\lambda' M_0(p = 0, \lambda') T^B(\lambda')]. \tag{3.7}$$

The distance modulus is modelled as a function of these SALT2 parameters, two new parameters $\boldsymbol{\delta} := (\alpha, \beta)$, and the peak absolute magnitude in B band M_B. If we define the corrected magnitude as

$$m_B^{corr}(\boldsymbol{\delta}) := m_B^\star + \alpha x_1 - \beta c, \tag{3.8}$$

we can write

$$\mu(\boldsymbol{\delta}, M_B) = m_B^{corr}(\boldsymbol{\delta}) - M_B. \tag{3.9}$$

Assuming that all Type Ia supernova events are independent, we can rewrite Eq. (3.6) in terms of the number of supernovae in the sample N as

$$\chi^2_{SALT2}(\boldsymbol{\theta}, \boldsymbol{\delta}, \mathcal{M}(M_B, h)) = \sum_{i=1}^{N} \frac{[\mu_i(\boldsymbol{\delta}, M_B) - \mu_{th}(z_i; \boldsymbol{\theta}, h)]^2}{\sigma_i^2(\boldsymbol{\delta}) + \sigma_{int}^2}, \tag{3.10}$$

where $\boldsymbol{\theta}$ represents the cosmological parameters other than h and $\mathcal{M}(M_B, h) := M_B + \mu_0(h)$. So the theoretical distance modulus is given by

$$\mu_{th}(z, \boldsymbol{\theta}, h) = 5\log[D_L(z; \boldsymbol{\theta})] + \mu_0(h). \tag{3.11}$$

The supernova intrinsic dispersions need to be accounted for and are added in quadrature to the distance modulus dispersion, given by

$$\sigma_i^2(\delta) = \sigma^2_{m_B^\star,i} + \alpha^2\sigma^2_{x_1,i} + \beta^2\sigma^2_{c,i} + 2\alpha\sigma_{m_B^\star,x_1,i} - 2\beta\sigma_{m_B^\star,c,i} - 2\alpha\beta\sigma_{x_1,c,i} + \sigma^2_{\mu,z,i}, \tag{3.12}$$

where $\sigma^2_{\mu,z,i}$ is the contribution to the distance modulus dispersion due to redshift uncertainties from peculiar velocities and also from the measurement itself. For simplicity and following Kessler et al. (2009b), this contribution will be modeled using the distance-redshift relation for an empty universe, so we have

$$\sigma_{\mu,z,i} = \sigma_{z,i}\left(\frac{5}{\ln 10}\right)\frac{1 + z_i}{z_i(1 + z_i/2)}, \tag{3.13}$$

where

$$\sigma^2_{z,i} = \sigma^2_{spec,i} + \sigma^2_{PV}. \tag{3.14}$$

$\sigma_{spec,i}$ is the redshift measurement error, and σ_{PV} is the redshift uncertainty due to peculiar velocity.

Astier et al. (2006) showed that by minimizing Eq. (3.10), a bias towards increasing values of α and β shows up. Guy et al. (2007) circumvent this problem with an iterative method, in which the χ^2 presented in Eq. (3.10) is replaced by

$$\chi^2_{SALT2}(\boldsymbol{\theta}, \boldsymbol{\delta}, \mathcal{M}) = \sum_{i=1}^{N} \frac{[\mu_i(\boldsymbol{\delta}, M_B) - \mu_{th}(z_i; \boldsymbol{\theta}, h)]^2}{\sigma_i^2(\eta) + \sigma_{int}^2}. \tag{3.15}$$

Since η is not a χ^2_{SALT2} parameter, it is given an initial value and the optimization is performed on $\boldsymbol{\theta}$, $\boldsymbol{\delta}$ and M. After this, η is updated with the best fit value of $\boldsymbol{\delta}$ and the optimization is performed again and again, until a convergence is achieved. During this process, σ_{int} is not considered a free parameter to be optimized, being determined rather by an initial value that will next perform the iterative procedure described above and the value of σ_{int} is then obtained by fine tuning it so that the reduced χ^2 equals unity (with all the other parameters fixed on their best fit values). The iterative procedure is repeated once more with this new value and the final best fit values are obtained.

Considering that the Type Ia supernova light curve fitting parameters are Gaussian distributed random variables, one can take as starting point the likelihood

$$L = \frac{1}{(2\pi)^N \det \Sigma} \exp(-X^T \Sigma^{-1} X/2), \tag{3.16}$$

which is related to the χ^2 in Eq. (3.6) by

$$\mathcal{L} := -2 \ln L = \chi^2 + \ln \det \Sigma + N \ln(2\pi). \tag{3.17}$$

One can note that, when the full covariance of the problem is known, minimizing χ^2 is equivalent to minimizing $\mathcal{L}$. However, this is not the case for current Type Ia supernova observations and neglecting one term in Eq. (3.17) would, in principle, lead to a biased result. In order to obtain probability distributions functions for all parameters, including σ_{int} and $\boldsymbol{\delta}$, we need to minimize the function

$$\mathcal{L}_{SALT2}(\boldsymbol{\theta}, \boldsymbol{\delta}, \mathcal{M}, \sigma_{int}) = \chi^2_{SALT2}(\boldsymbol{\theta}, \boldsymbol{\delta}, \mu, \sigma_{int}) + \Sigma_i^N \ln(\sigma_i^2(\boldsymbol{\delta}) + \sigma_{int}^2), \tag{3.18}$$

where parameter-independent terms were neglected. $\chi^2_{SALT2}(\boldsymbol{\theta}, \boldsymbol{\delta}, \mathcal{M}, \sigma_{int})$ is given by Eq. (3.10), considering σ_{int} as a free parameter.

The most common constraints analyzed are the 68% and 95% confidence level contours in the planes: 1) $\Omega_{m0} \times \Omega_{\Lambda 0}$ (for the ΛCDM model), 2) $\Omega_{m0} \times w$ (for the FwCDM model), and 3) $w \times w_a$. Examples of those three cases can be seen in Figures (3.3) and (3.4), from Betoule et al. (2014).

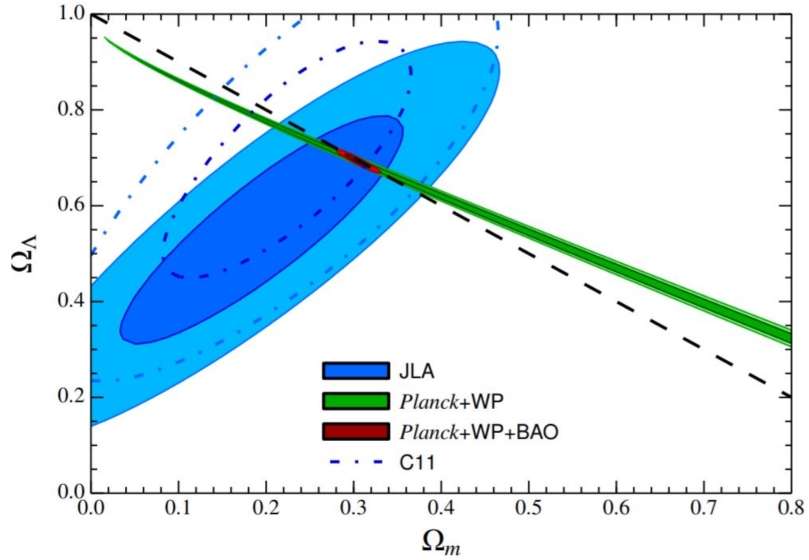

Figure 3.3: 68% and 95% confidence contours (including systematic uncertainty) for the Ω_m and Ω_Λ cosmological parameters for the o-ΛCDM model. Labels for the various data sets correspond to the JLA supernova compilation (JLA), the Conley (2011) Type Ia supernova compilation (C11), the combination of Planck temperature and WMAP polarization measurements of the CMB fluctuation (Planck+WP), and a combination of measurements of the BAO scale (BAO). The black dashed line corresponds to a flat universe. Credits: Betoule et al. (2014).

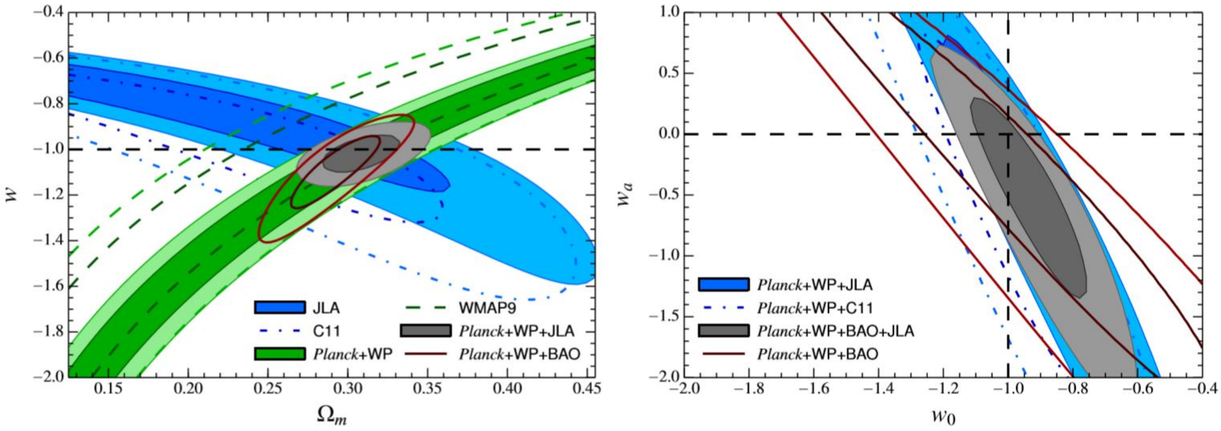

Figure 3.4: Confidence contours at 68% and 95% for the Ω_m and w cosmological parameters for the flat wCDM model in the left, and for w and w_a in the right. The black dashed line corresponds to the cosmological constant hypothesis. Credits: Betoule et al. (2014).

3.4 Supernova Peculiar Velocities

As explained in the previous sections, in order to constrain cosmological parameters (namely Ω_m and w for a flat universe) using supernova data, one needs to account for the dispersions of these objects that are not due to the expansion of the Universe. These dispersions include the supernova peculiar velocities related to the distribution of matter in the large-scale structure, which are often just modeled as Gaussian random terms.

However, it has been shown in Gordon et al. (2007) that supernova velocities are not really random, as the large-scale gravitational potential wells incur in coherent velocity flows. This means that any two supernovae in the same region of the sky (which extends to many dozen of Mpc) are supposed to have correlated magnitude fluctuations. In other words, if a given supernova is dimmer than the average because it is moving away from us, a nearby supernova has an excess probability of also being dimmer than the average because it will be in the same velocity flow. Figure (3.5) exemplifies it.

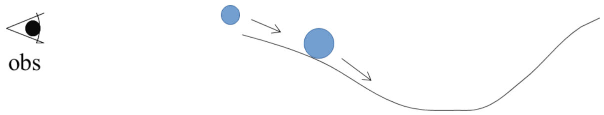

Figure 3.5: Representation of two supernovae falling in the same large-scale structure potential well.

Castro et al. (2016) showed this correlation through Figure (3.6), that represents 3 random realizations of 500 idealized supernovae, i.e., considering that the only dispersion they have is due to the peculiar velocity fields. This way, one can easily notice the magnitude correlations by eye, although in practice these are suppressed by much larger intrinsic dispersion of the supernovae.

As emphasized by Hui & Greene (2006), in the limit of low redshift ($z \lesssim 0.1$) and large sample size, these correlations between supernova peculiar velocities contribute significantly to the overall error budget related to the estimation of cosmological parameters. Gordon et al. (2007) calculated the ratio of the covariance from peculiar velocities compared to the random errors for a pair of supernovae over a range of angular separations in Figures (3.7) and (3.8).

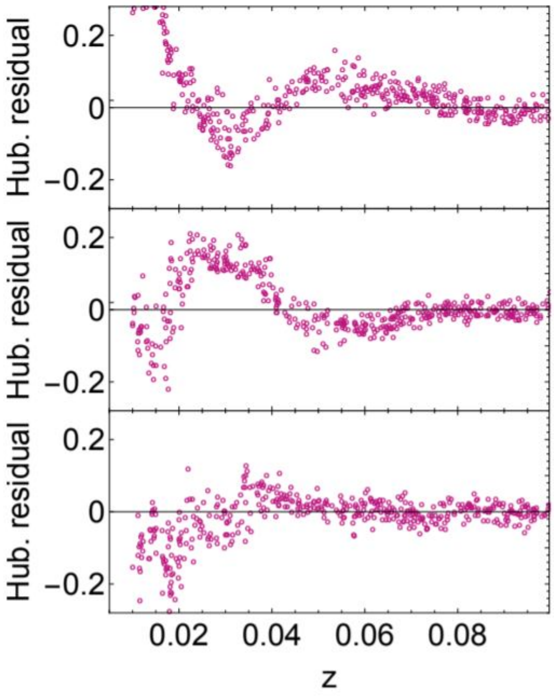

Figure 3.6: 3 random realizations of 500 idealized supernovae. In practice, these are suppressed by much larger intrinsic dispersion of the supernovae. Credits: Castro et al. (2016)

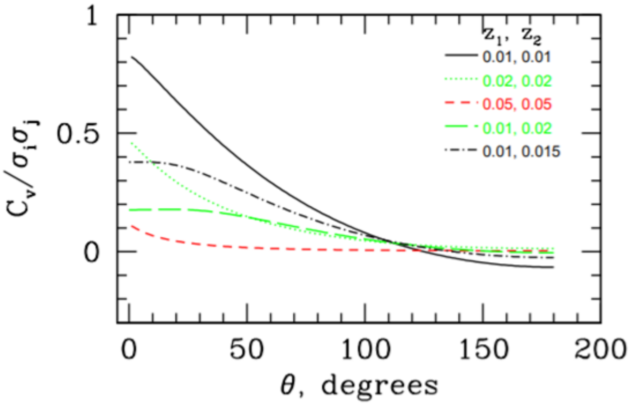

Figure 3.7: C_v^{PV} compared to the random errors σ for 2 supernovae over a range of angular separations θ. Credits: Gordon et al. (2007)

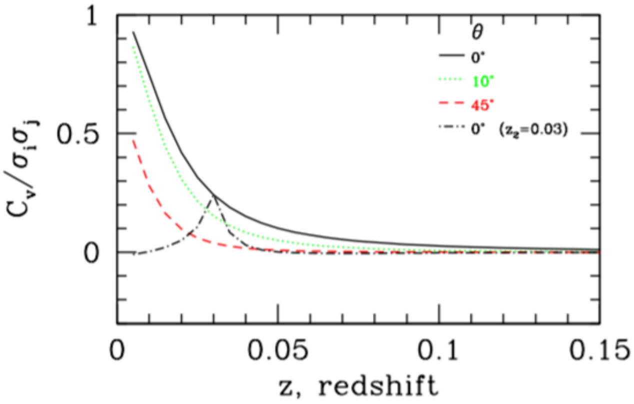

Figure 3.8: The same as Figure (3.7), but varying z, with both supernovae at the same z or with one supernova fixed at $z = 0.03$ (dash-dot). Credits: Gordon et al. (2007)

A way of accounting for the correlated peculiar velocities is to estimate the underlying density field from galaxy redshift surveys and then use this to try and remove peculiar velocity at each supernovae. However, instead of just taking it off of the analysis, we can use the correlation between these velocities to constrain perturbation parameters.

The effect of peculiar velocities leads to a perturbation in the luminosity distance (δD_L) given by

$$\frac{\delta D_L}{D_L} = \hat{x} \cdot \left(\boldsymbol{v} - \frac{(1+z)^2}{H(z)D_L} [\boldsymbol{v} - \boldsymbol{v_0}] \right), \tag{3.19}$$

where $\hat{x}$ is the position of the supernova at redshift z, and $\boldsymbol{v_0}$ and $\boldsymbol{v}$ are the peculiar velocities of the observer and supernova respectively. The CMB dipole can correct for $\boldsymbol{v_0}$. This way, a supernova survey can estimate the projected peculiar velocity field.

The velocity correlation function is defined by

$$\xi(x_i, x_j) \equiv \langle (\boldsymbol{v}(x_i) \cdot \hat{x}_i)(\boldsymbol{v}(x_j) \cdot \hat{x}_j) \rangle. \tag{3.20}$$

Since the velocity correlation function must be rotationally invariant, it can be decomposed into the components (Dodelson 2003):

$$\xi(x_i, x_j) = \sin\theta_i \sin\theta_j \xi_\perp(x, z_i, z_j) + \cos\theta_i \cos\theta_j \xi_\parallel(x, z_i, z_j), \tag{3.21}$$

where $x_{ij} \equiv x_i - x_j$, $x = |x_{ij}|$, $\cos\theta_i \equiv \hat{x}_i \cdot \hat{x}_{ij}$ and $\cos\theta_j \equiv \hat{x}_j \cdot \hat{x}_{ij}$. In linear theory, those components are given by (Dodelson 2003):

$$\xi_{\parallel,\perp} = G'(z_i)G'(z_j) \int_0^\infty \frac{dk}{2\pi^2} P(k) K_{\parallel,\perp}(kx), \tag{3.22}$$

where G is the growth function, and for an arbitrary value of y, $K_\parallel(x) \equiv j_0(x) - \frac{2j_1(x)}{x}$ and $K_\perp(x) \equiv \frac{j_1(x)}{x}$, and j_0, j_1 represent the spherical Bessel functions. For the diagonal $i = j$ terms, we have simply

$$\xi(x_i, x_i) = [G'(z_i)]^2 \int_0^\infty \frac{dk}{2\pi^2} \frac{P(k)}{3}. \tag{3.23}$$

The peculiar-motion convariance matrix is then given by

$$C_v(i,j) = \left[1 - \frac{(1+z_i)^2}{H(z_i)d_L(z_i)} \right] \left[1 - \frac{(1+z_j)^2}{H(z_j)d_L(z_j)} \right] \xi(x_i, x_j). \tag{3.24}$$

Since the amplitude of the correlations between supernova peculiar velocities is directly related to the 2-point correlation function of matter, it can also provide the matter power spectrum, from which we can derive the standard deviation of density perturbations on 8 Mpc/h (σ_8) based on (Eq. 2.40). If we extend the analysis for beyond the ΛCDM model, we can account for the free parameter γ that represents the common parametrization for the linear growth rate, which can be calculated using (Eq. 2.41). Within General Relativity and for the ΛCDM model, $\gamma = \gamma_{\Lambda CDM} \approx 0.55$. γ does not depend strongly on the equation of state parameter of dark energy, so it is often employed as a simple way of describing the growth rate in modified gravity models.

Both peculiar velocity fields and gravitational lensing can put constraints on σ_8 x γ, and they provide complementary constraints on this matter. Figure (3.9) shows a forecast by Castro et al. (2016) for a possible future catalog, counting on 3000 supernovae from DES plus 1000 low-redshift supernovae in $0.01 < z < 0.1$, in an area of the sky of 400 deg^2. One can see that lensing and peculiar velocity analysis show an angle between degeneracies of $\sim$60 deg, what expresses good complementarity.

Figure (3.10) shows a comparison among the constraints on σ_8 and γ from supernovae (using lensing and peculiar velocities), Planck CMB spectra, clusters and galaxies. Note that the JLA supernova data is already able to complement well the others, specially the CMB. Planck CMB spectra constrains well σ_8 supposing $\gamma = \gamma_{\Lambda CDM} \approx 0.55$, but needs complement when γ is a free parameter.

Castro et al. (2016) also presented constrains on the values of σ_8 (using a fixed value for γ), and γ (fixing the perturbation parameters $\Omega_{b,0}$, H_0, A, n_s, τ), showed in Figure (3.11). Those both analysis are well motivated because: 1) supposing General Relativity as the correct theory for gravitation, γ is fixed; 2) if we rely on other precise measurements of the perturbation parameters, there is no difference in practice between marginalizing over the priors or fixing them to the best fit. Huterer et al. (2015) found similar results.

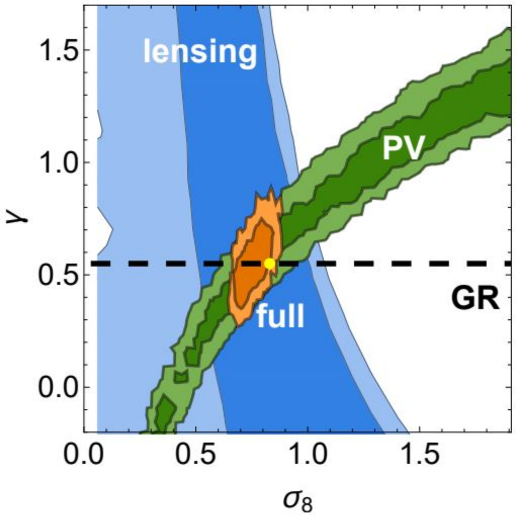

Figure 3.9: 1 and 2σ forecast for a possible future supernovae catalog of 3000 DES + 1000 low-redshift supernovae in $0.01 < z < 0.1$, in an area of the sky of 400 deg^2. The contours were obtained by using peculiar velocities (in green), lensing (in blue), or both combined (in orange). The dashed black line represents the expectation from general relativity and the yellow dot represents the considered value in ΛCDM. Credits: Castro et al. (2016)

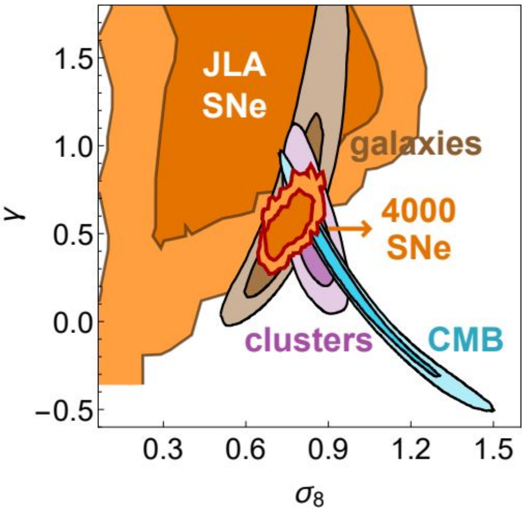

Figure 3.10: A comparison among the constraints on σ_8 and γ from supernovae (using lensing and PV), Planck CMB spectra, clusters and galaxies. The large orange contours are from the JLA supernovae, whereas the smaller orange contours with red borders are a forecast for DES + 1000 low-z supernovae. The other contours were obtained by Mantz et al. (2015). Credits: Castro et al. (2016)

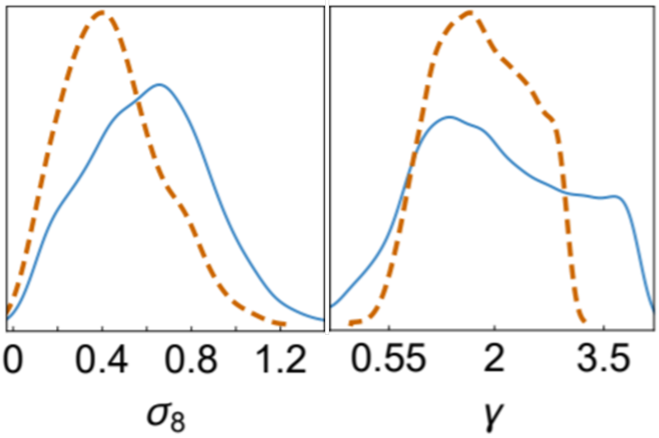

Figure 3.11: Marginalized 1-dimensional constraints on σ_8 and γ from the combination of supernova lensing and peculiar velocities. In blue, the full results; in dashed brown, the contours obtained by assuming General Relativity ($\gamma = 0.55$; left) or all perturbation quantities in $P(k)$ (right). Credits: Castro et al. (2016)

Some upcoming surveys, such as the DES and LSST, will have a great focus on lensing, what will contribute to better constrain the blue area in Figure (3.9). So we are going to need efficient survey strategies in order to also constrain those parameters using supernova peculiar velocities. The challenging aspect is that peculiar velocities of ~ 300 km/s are typically much smaller than the Hubble expansion velocity; the two are similar in value only at the very lowest redshifts, $z \sim 0.001$. In the next chapter, we investigate how the duration, depth and field size of supernova surveys influence on the peculiar velocity signals and estimation of σ_8 and γ from that.

Chapter 4

Optimizing Observations

Chapters 2 and 3 showed that the use of peculiar velocity fields to constrain perturbation parameters is very important, first because lensing alone will not be able to put good constraints on σ_8 x γ (Castro et al. 2016); and also because the σ_8 estimates we have until now (from Planck Collaboration (2016)), already considered very precise, were derived using a fixed value for γ (as it is in ΛCDM). Peculiar velocities are very sensitive to σ_8 and γ, allowing the latter to be a free parameter.

The objective of this work was to understand which observational parameters are more sensitive to the peculiar velocity field signals from supernovae. In order to do that, we used the pairV code (Hui & Greene 2006) to account for the magnitude covariance matrix in our simulated supernova catalogs, which were constructed with varying sky areas, survey durations and depths. Then we considered some priors and a matter power spectrum evaluated numerically using CAMB (Lewis et al. 2010) to constrain σ_8 and γ.

4.1 Simulations

Since the first objective of this work was to make comparisons among survey parameters, we used supernova simulations based on idealized surveys: whose observations are able to detect all supernovae exploded in a certain volume, regardless of how distant they are.

To generate the mock catalogs, we first assumed a magnitude distribution given by a fiducial ΛCDM model in General Relativity (i.e., $\gamma = 0.55$) with $\sigma_8 = 0.83$, $\Omega_{m0} = 0.3$ and $h = 0.7$. Then we added the peculiar velocity effects, employing the pairV code to compute the covariance, and an intrinsic dispersion of $\sigma_{int} = 0.13$ mag to the diagonal of the covariance matrix. The resulting covariance was used to draw random realizations of a Gaussian.

We first simulated the mother catalogs: 40 versions of 6-year catalogs, covering an area of 600 deg^2 and reaching redshift 0.25. Assuming a constant supernova explosion rate of 3 x 10^{-5}/yr/Mpc^3 (Rodney et al. (2014) and Cappellaro et al. (2015)), this totalizes 11,285 supernovae. We later divided these catalogs in children catalogs with different field areas, survey durations and maximum redshifts, so that we could estimate σ_8 and γ with each and see how the measurements scale with survey time, area and redshift.

The variations of time were taken by randomly picking supernovae from the mother catalogs. For the 1-year catalogs, we took 11285/6 supernovae; for the 2-year ones, we took 2x11285/6, etc. Given that, we constructed 40 versions of 5 children catalogs of 1, 2, 3, 4 and 5 years, covering the whole 600 deg^2 survey area. Figure (4.1) illustrates it.

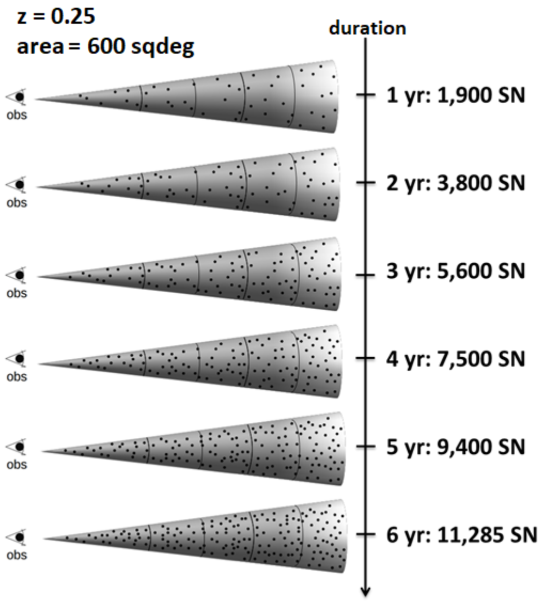

Figure 4.1: Representation of the different duration children catalogs used in our studies. Area and redshift are fixed while time is varying. We simulated 40 versions of each.

For the area variations, we sampled 2 subareas by taking 300 deg^2 and 450 deg^2 from the central region of the 600 deg^2 catalogs, and produced 2x40 children catalogs (40 for 300 deg^2 + 40 for 450 deg^2) representing surveys with 6 years of duration and reaching $z = 0.2$. We decided to make this analysis up until $z = 0.2$ instead of $z = 0.25$ because we had already noticed that this upgrade in the redshift would not bring much more information for the results, so it would be unnecessarily time-consuming. Figure (4.2) illustrates the area variations.

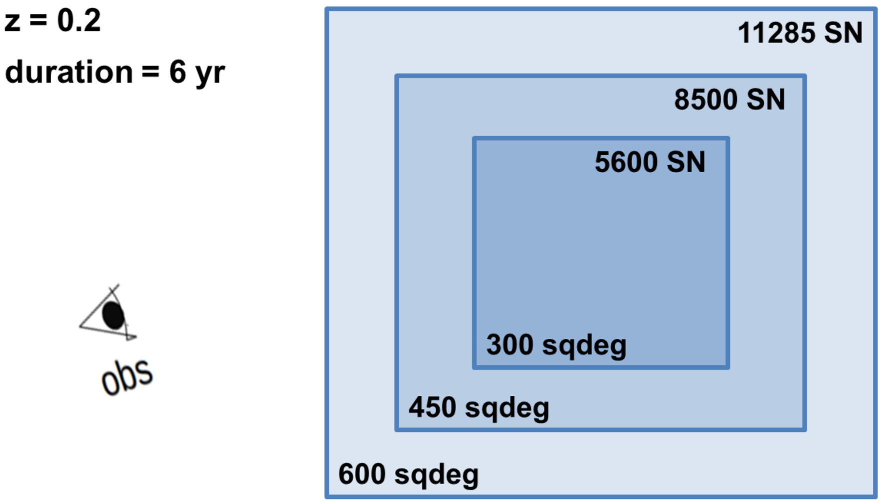

Figure 4.2: Representation of the different area children catalogs used in our studies. Duration and redshift are fixed while the solid angle from which is being observed is varying. We simulated 40 versions of each.

We also made variations in the redshift (that represents the depth). So we had 40 full-area, full-time children catalogs reaching z = 0.05 (which contains 70 SN), other 40 reaching z = 0.1 (700 SN), and the same for z = 0.15 (2500 SN) and z = 0.2 (5800 SN). Figure (4.3) illustrates it, and Table (4.1) sums up the subcatalogs we considered in the analysis.

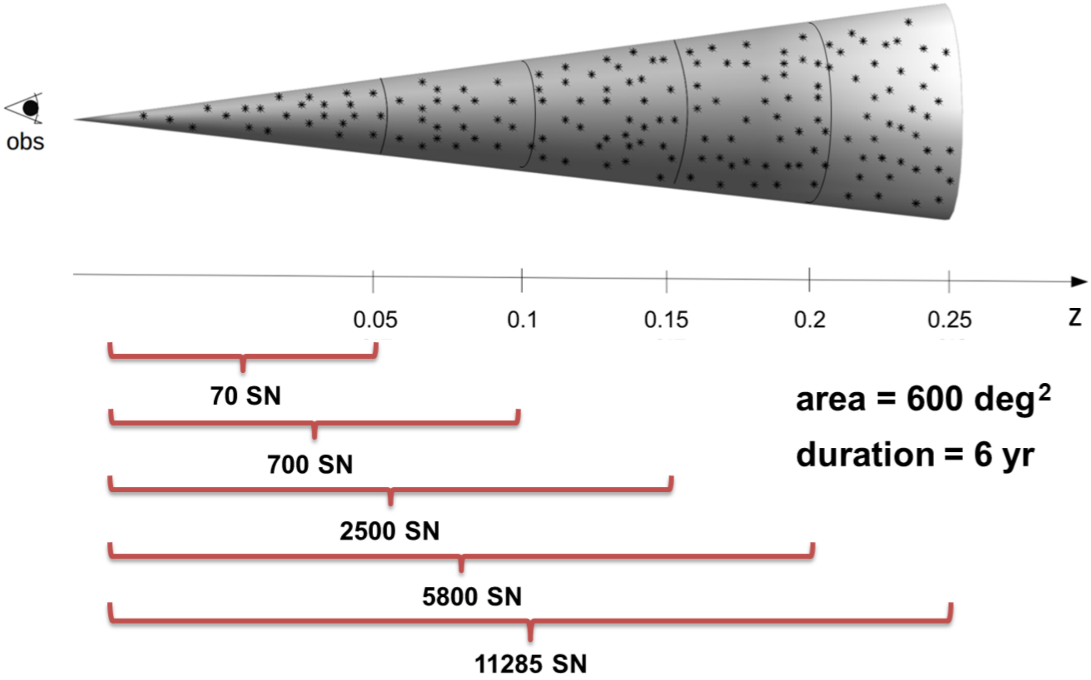

Figure 4.3: Representation of the different redshift children catalogs used in our studies. Area and duration are fixed while depth is varying. We simulated 40 versions of each.

Mother catalogs: 40 versions of 6 yr, 600 deg^2, up to $z = 0.25$ complete survey, with total 11,285 SNe Ia
Children catalogs:
. Durations: 1, 2, 3, 4 and 5 yr
. Areas: 300 and 450 deg^2
. Max. redshifts: 0.05, 0.1, 0.15 and 0.2

Table 4.1: Survey duration, total area and maximum redshift considered in our analysis.

4.2 Determination of σ_8

We constrained the value of σ_8 for each of the 6x40 different-time catalogs and 3x40 different-area catalogs, considering only the supernovae up to 5 different values of redshift: 0.05, 0.1, 0.15, 0.2 and 0.25. In order to estimate the value of σ_8, we used the likelihood function:

$$L_{PV} \propto \frac{1}{\sqrt{|C_{ij}^{PV}|}} \exp\left[-\frac{1}{2}\delta_m^T (C_{ij}^{PV})^{-1}\delta_m\right], \tag{4.1}$$

where $\delta_m = \sigma_8 - \sigma_{8,fid}$.

The matter power spectrum was evaluated numerically using CAMB (Lewis et al. 2010) in a 1-dimensional parameter space sampled by a grid. Since our objective is to make comparisons between survey strategies, there's no need to let all parameters besides A_s (the amplitude of scalar fluctuations) - directly related to σ_8 - free, so we assumed a model with the same background expansion as a flat ΛCDM, composed of A_s and the 6 following parameters as priors: $\Omega_{c0} = 0.254$, $\Omega_{b0} = 0.046$, $\gamma = 0.55$, $h = 0.7$, $n_s = 0.9603$, $\tau = 0.089$. Those values were taken from Bennett et al. (2014), Planck Collaboration (2016) and Iocco et al. (2009), where h is H_0 in units of 100 km/s/Mpc and $\Omega_{m0} \equiv \Omega_{c,0} + \Omega_{b0}$. From the resulting matter power spectrum $P(k)$, we derive the standard deviation of density perturbations on 8 Mpc/h spheres: Eq. (2.40).

Figure (4.4) shows an example of contraints on σ_8. It was constructed based on one of the 40 versions of the full-area catalog (600 deg^2), for 6 years of survey, and reaching $z = 0.15$. Since we made a cut in 0, not allowing σ_8 constraints to be negative, some likelihood curves are partially Gaussian-like. Figure (4.5) shows an example of this case, from another version of the full-area, 6-year survey, with a cut in $z = 0.2$.

Although this cut is physically justified as σ_8 cannot be negative, such oscillation in the likelihood just happens due to large fluctuations when there is a small number of supernovae in the chosen sample. So the standard deviations for low-z, low-area and low-time surveys will sometimes appear to be lower or of the same order of high-z, wide, long-time surveys. This effect could hinder the comparisons we need to make. Besides that, if we want to make an analysis that lies on the Fisher matrix (see Section 4.3), we need to assume Gaussianity. That is why, in the following sections, we are going to use Gaussian fits (as exemplified in Figures (4.6) and (4.7)) to analyze the sensitiveness of each observational parameter on the estimation of σ_8. In Appendix A one can see a comparison between both analysis: the one using the real likelihood curves and another using the Gaussian fits to them.

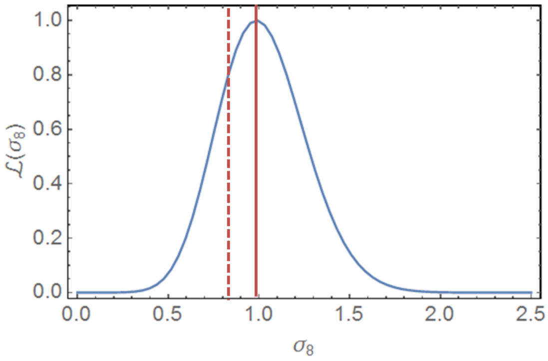

Figure 4.4: σ_8 likelihood curve for a hypothetical survey that covers 600 deg^2, reaches $z = 0.15$ and lasts 6 years. The red lines represent the best fit (solid) and fiducial (dashed) values.

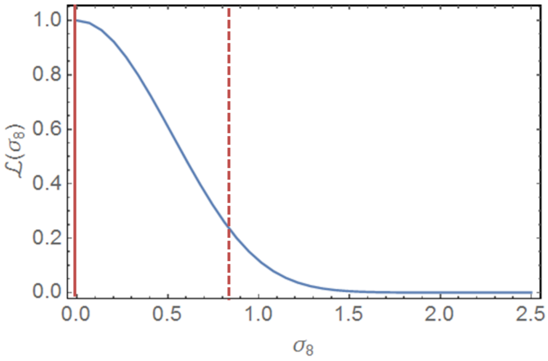

Figure 4.5: σ_8 likelihood curve for a hypothetical survey that covers 600 deg^2, reaches $z = 0.2$ and lasts 2 years. The red lines represent the best fit (solid) and fiducial (dashed) values.

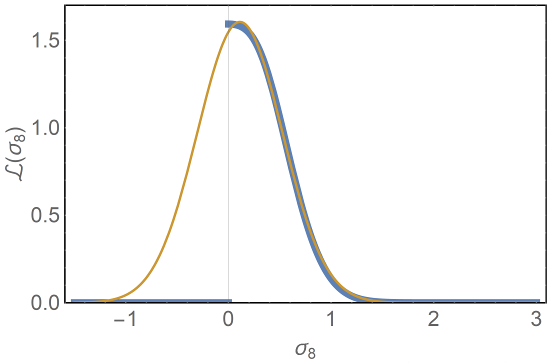

Figure 4.6: σ_8 likelihood curve (in blue) and Gaussian fit (in yellow) for a hypothetical survey that covers 600 deg^2, reaches $z = 0.15$ and lasts 2 years.

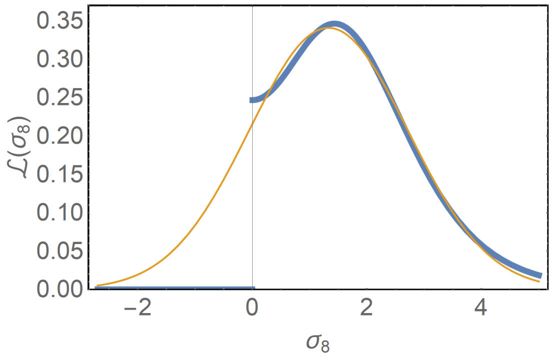

Figure 4.7: σ_8 likelihood curve (in blue) and Gaussian fit (in yellow) for a hypothetical survey that covers 600 deg^2, reaches $z = 0.05$ and lasts 1 year.

4.3 Comparing Parameters

In order to predict the role of each observational parameter on the estimation of cosmological ones, we are going to make use of the Fisher matrix, which is a way of measuring the amount of information that an observable random variable carries about an unknown parameter of a distribution that models it. The accuracy with which cosmological parameters can be measured from a given data set is conveniently computed with the Fisher information matrix formalism (see Tegmark et al. (1997) for a review) defined as

$$F_{lm} \equiv - \left\langle \frac{\partial^2 \ln f}{\partial p_l \partial p_m} \right\rangle , \tag{4.2}$$

where f depends on a vector of p_l and p_m, which represent hypotetical cosmological parameters to be estimated. The inverse of the Fisher matrix (F^{-1}) can be interpreted as the best possible covariance matrix for the measurement errors on the parameters. No unbiased method whatsoever is able to measure the l^{th} parameter with standard deviation less than $1/\sqrt{F_{ll}}$.

In the case of an experiment that measures the matter power spectrum, the integral form of the Fisher matrix is given by Tegmark (1997) and Seo & Eisenstein (2003):

$$F_{lm} = \frac{1}{8\pi^2} \int_{-1}^{+1} d\mu \int_{k_{min}}^{k_{max}} k^2 dk \frac{\partial \ln P(k,\mu)}{\partial p_l} \frac{\partial \ln P(k,\mu)}{\partial p_m} \left[\frac{nP(k,\mu)}{nP(k,\mu)+1} \right]^2 V_{survey}, \tag{4.3}$$

where μ is the cosine of the observed angle, k represents the scale, $P(k,\mu)$ is the matter power spectrum, n is the number density of supernova in this region, and V_{survey} is the total volume observed by the survey.

In the following sections, we are going to present how the error related to the estimation of cosmological parameters behaves with varying survey areas, durations and redshifts, and interpret them in light of the Fisher matrix analysis.

4.3.1 Redshift

One can see in Eq. (4.3) that a Fisher matrix F_{ll} is proportional to the survey volume V_{survey}. If we take a infinitesimal redshift bin, we can say that $dV_{survey} = A(z)dz$. Since the area $A(z)$ is proportional to z^2, this means that $V_{survey} \propto z^3$ and then $F_{ll} \propto z^3$. So the minimum achieved error is $\sigma = 1/\sqrt{F_{ll}} \propto z^{\alpha}$, where $\alpha = -3/2$.

The relation above, stating that the error falls with $z^{3/2}$, would be valid if all supernovae had the same statistical significance. However, the contribution of peculiar velocities in the measurement of supernova magnitudes decreases with redshift, as the contribution from cosmic expansion grows. One way of accounting for this effect would be by taking the ratio of peculiar flow to Hubble flow to use this as a weight on peculiar velocity determinations - the lower the supernova redshift, the higher the weight. Typical peculiar velocities are of the order of 300 km/s, and so the ratio at $z = 0.1$, for example, is about $300/(3 \times 10^5 \times 0.1) \sim 0.01$, using $c = 3 \times 10^5$ km/s. Translating this into fluctuations in magnitude, we have $\delta m_{z=0.1} \sim 2.17 \times 0.01 \sim 0.02$. At $z = 0.2$, the ratio is $300/(3 \times 10^5 \times 0.2) \sim 0.005$, so in this case: $\delta m_{z=0.2} \sim 2.17 \times 0.005 \sim 0.01$. Since the intrinsic spread in supernova magnitudes is the order of $(0.1 - 0.15)$ - much higher than δm -, it is common in the literature to ignore peculiar motion. However, this argument misses that the correlations in magnitude fluctuations between supernovae do not only introduce a negligible Poissonian scatter, but also a correlated component that needs to be taken into account.

Hui & Greene (2006) and Gordon et al. (2007) consider that the correlations between supernova peculiar velocities contribute significantly to the overall error budget only up to $z \lesssim 0.1$. In order to study the effect of the redshift limit, which represents the depth of a given survey, we used our sample of 11,285 supernovae distributed in 600 deg^2 to perform the likelihood estimations for σ_8, and present, in Figure (4.8), $\sigma_{mean}(\sigma_8)$ as a function of maximum redshift for different survey durations, where $\sigma_{mean}(\sigma_8)$ is the σ_8 error mean value of the 40 versions for each subcatalog of time variations. Figure (4.9) shows a similar analysis, but plotted by first tracing best fits for each version in a log-log plot and later taking the mean value and standard deviations of the inclinations. One can see in those figures that it is possible to gain information on the estimation of σ_8 by going further, until $z = 0.2$. Beyond this redshift value, it shows that the decrease in the standard deviation starts to become negligible.

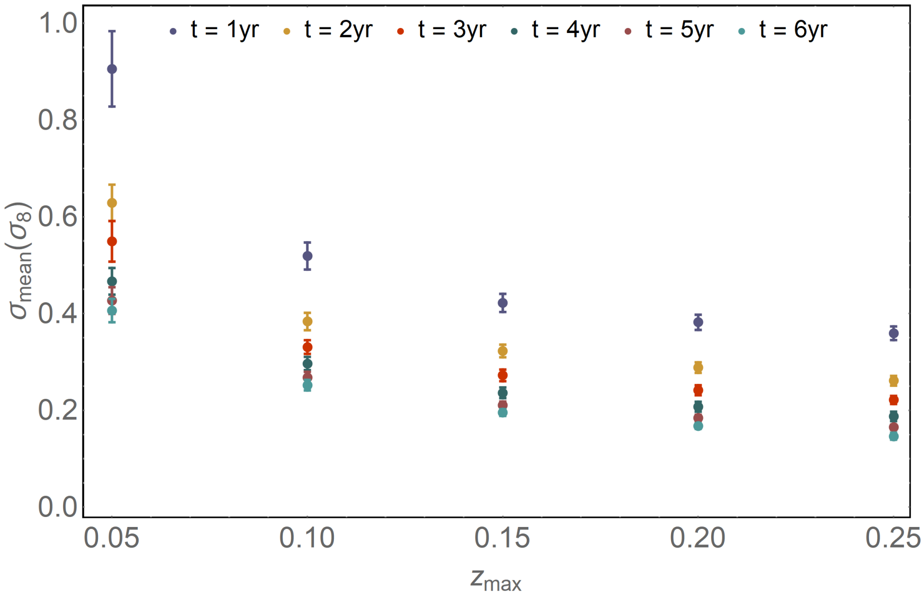

Figure 4.8: The standard deviation of σ_8 with 2σ error bars as a function of the maximum redshift, for the different survey durations indicated.

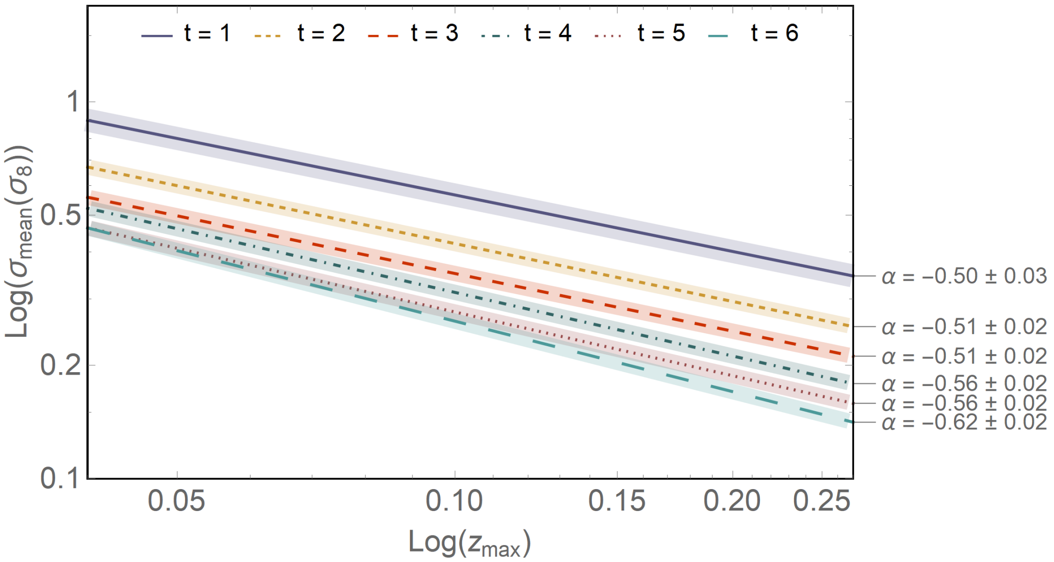

Figure 4.9: Log-log analysis for the error of σ_8 for different survey durations as a function of the maximum redshift performed by taking the average of the inclinations of all the versions.

4.3.2 Survey Duration

The survey duration is an important observational parameter to analyze. It may seem plausible to think that the longer we observe, the more information we have. However, when we are looking at peculiar velocity fields, we gain information when raising the survey time in the beginning, but it gets to an apex and the gain of information starts declining after some time, meaning that all the information about the clumpiness of determined region is getting saturated. Any other detected supernova will not make any difference since the peculiar velocity correlations driven by previously detected supernova already tell all that can be known from a given survey about a considered region.

The last factor in Eq. (4.3),

$$V_{eff} = \left[\frac{nP(k,\mu)}{nP(k,\mu)+1}\right]^2 V_{survey}, \tag{4.4}$$

can be seen as an effective survey volume. It is worth evaluating the two limiting cases for $nP(k,\mu)$. When $nP(k,\mu) >> 1$, it means that the sampling is good enough to derive all the cosmological information that can be extracted from the survey; in other words, detecting more supernovae will not bring any advantage. And when $nP(k,\mu) << 1$, the effective volume is severely reduced, meaning that even a small amount of supernova added can bring a lot of information. In particular, we see in this case that $F_{lm} \propto V_{eff} \propto n^2$. Since $F_{lm} \propto 1/\sigma^2$, we see that in this limit $\sigma \propto 1/n$. We can extend this analysis to the time parameter as the number of supernova detected is directly proportional to the duration of the survey; the number density increases with survey time for a fixed observed area. So we can conclude that we gain information by raising the survey time until it gets saturated. This tendency can be seen in Figure (4.10), that represents the Fisher matrix error for varying supernova number densities.

As our sample includes 11,285 supernovae distributed in 600 deg^2 up until redshift 0.25, this means a number density of about 5×10^{-4} SN h^3/Mpc^3 for the 6 years of survey. Figure (4.11) shows a plot with vertical lines representing the number density of supernovae for 1, 2, 3, 4, 5 and 6 years of survey, from left to right. Dashed lines represent power laws of the form $\sigma = (n_{SN})^{\alpha}$. In green we represent a power law with $\alpha = -1$ (indicated as "-1 inclination" in the plot), and in red $\alpha = -1/2$ ("-1/2 inclination" in the plot), that serve as reference for the rate of gained information as we move along the x-axis. One can note that, theoretically, our data is close to the -1/2 inclination curve. Given that, we expect that a log-log graph relating the error on σ_8 measurements with the survey's duration, for this sample, would show an inclination around -1/2, meaning that it is still worth continuing the survey in this field.

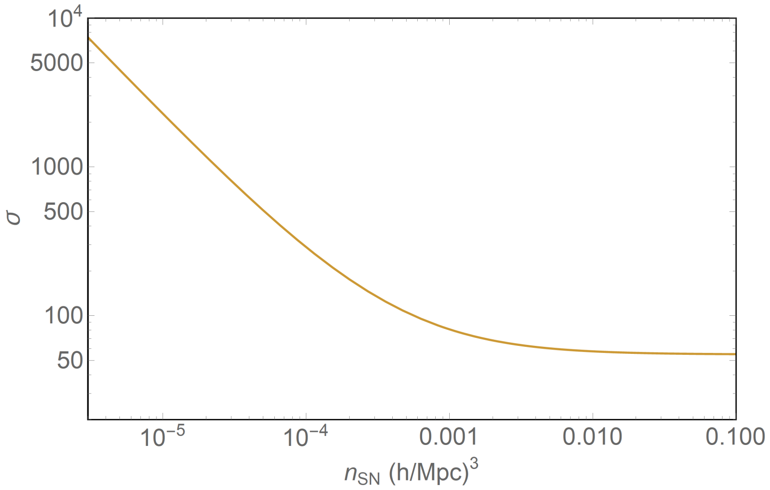

Figure 4.10: Fisher matrix error as a function of the number density of observed supernovae.

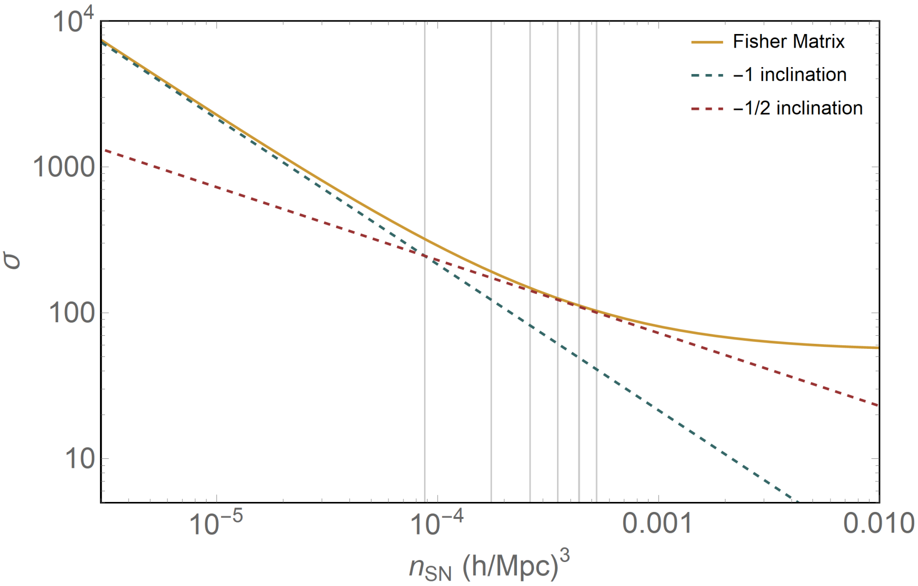

Figure 4.11: Fisher matrix error as a function of the number density of observed supernovae with gridlines representing different survey durations. From the left to the right, the vertical grid lines represent 1 to 6 years of the 600 deg^2 survey, reaching $z = 0.25$.

To exemplify with real upcoming surveys, Figures (4.12) and (4.13) show the same analysis applied to DES and LSST strategies. One can see that even after the intended time for these surveys (5 years for DES and 10 years for LSST), the power law is still steeper than $-1/2$, which means that observing longer the same field is much better than extending the observation to another area, since σ follows a fixed $-1/2$ index power law as a function of the area (see Section 4.3.3).

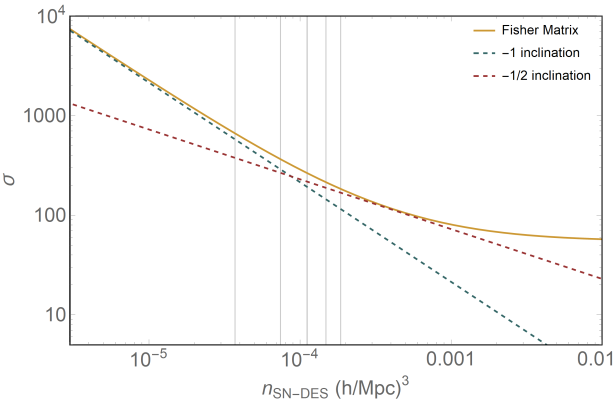

Figure 4.12: Fisher matrix error in function of the number density of observed supernovae with gridlines representing different survey durations for DES. From the left to the right, the vertical grid lines represent 1 to 5 years survey, reaching $z = 0.25$.

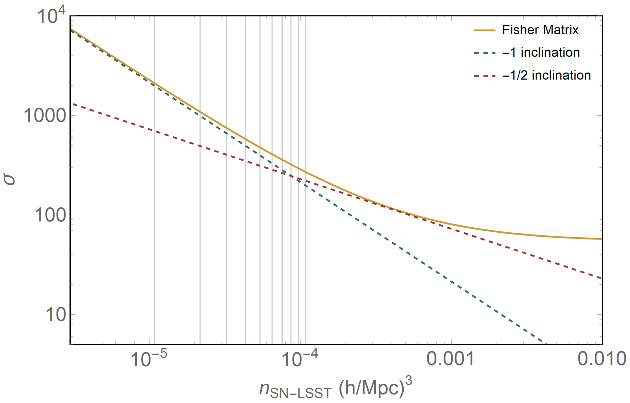

Figure 4.13: Fisher matrix error in function of the number density of observed supernovae with gridlines representing different survey durations for LSST. From the left to the right, the vertical grid lines represent 1 to 10 years survey, reaching $z = 0.25$.

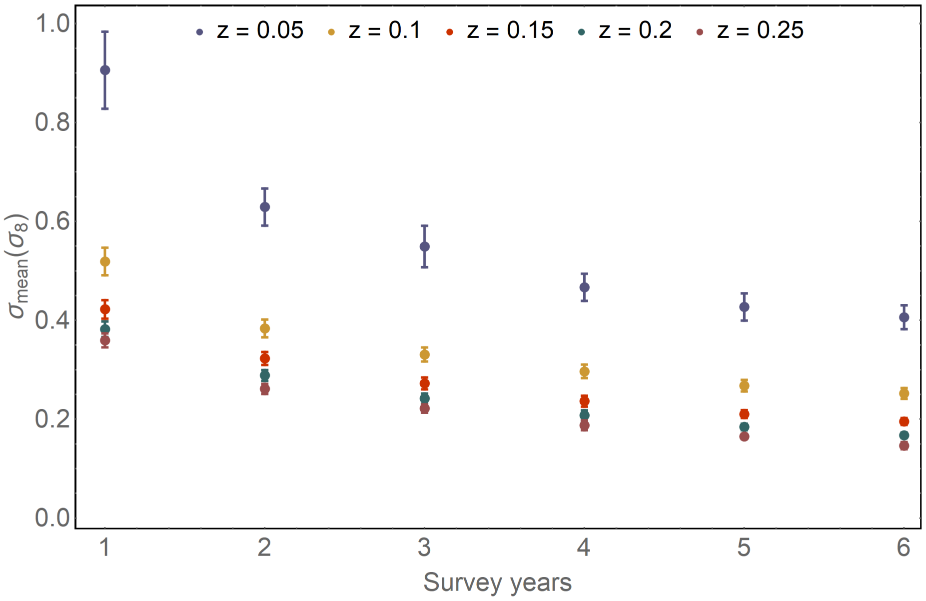

Figure 4.14: The standard deviation of σ_8 with 2σ error bars as a function of the survey duration, for the different redshift limits indicated.

In order to see this effect in practice, we performed the likelihood estimations for σ_8 based on our 11,285-supernovae sample and plotted Figure (4.14), that shows how $\sigma_{mean}(\sigma_8)$ changes with survey duration for different redshift limits, where $\sigma_{mean}(\sigma_8)$ is the σ_8 error mean value of the 40 versions for each subcatalog of time variations. Figure (4.15) shows a similar analysis, but plotted by first tracing best fits for each version in a log-log plot and later taking the mean value and standard deviations of the inclinations. Note that all the curves in Figure (4.15) are less inclined than the $-1/2$ index power law, meaning that it is in accordance with our predictions and it is still worth continuing the survey for a longer time.

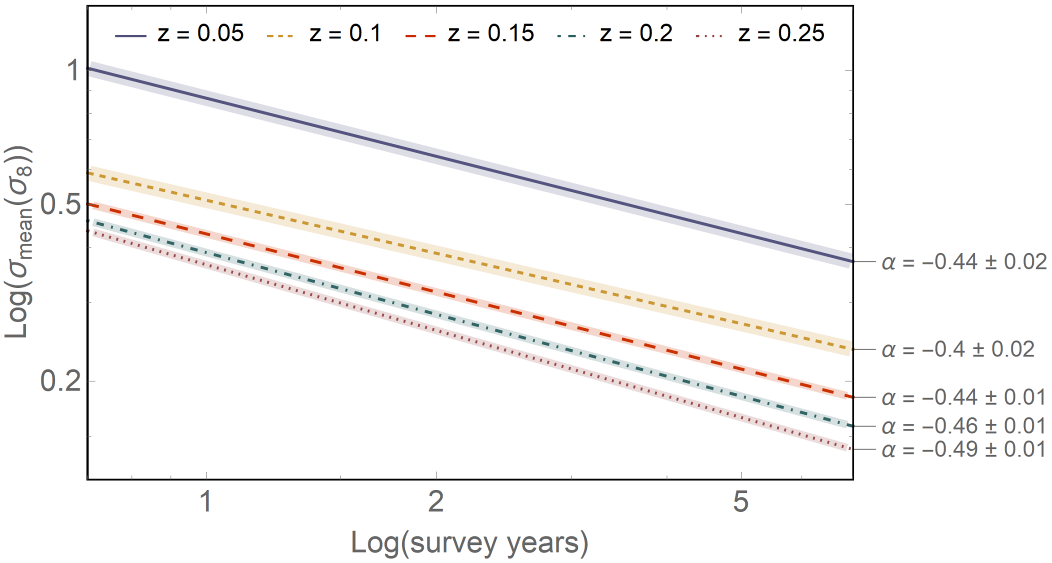

Figure 4.15: Log-log analysis for the error of σ_8 for different redshift limits as a function of the survey time performed by taking the average of the inclinations of all the versions.

4.3.3 Area of the Sky

The area case is trivial: since $F_{ll} \propto V_{survey}$, and $V_{survey} = \chi^3 \times \Omega/3$ (where Ω is the solid angle representing the sky area being observed and χ is the comoving distance), it means that $F_{ll} \propto \Omega$. So we have that $\sigma = 1/\sqrt{F_{ll}} \propto \Omega^{-1/2}$. As in the other cases, we have Figure (4.16) showing how the standard deviation of σ_8 changes with survey area by taking the average and error of the 40 versions for each time, and Figure (4.17), where we log-log plotted the 40 inclinations for each time and then took their average and error. One can see that this result is in accordance with our predictions as the different inclination values for different redshifts can be interpreted as statistical fluctuations around $\alpha = -1/2$.

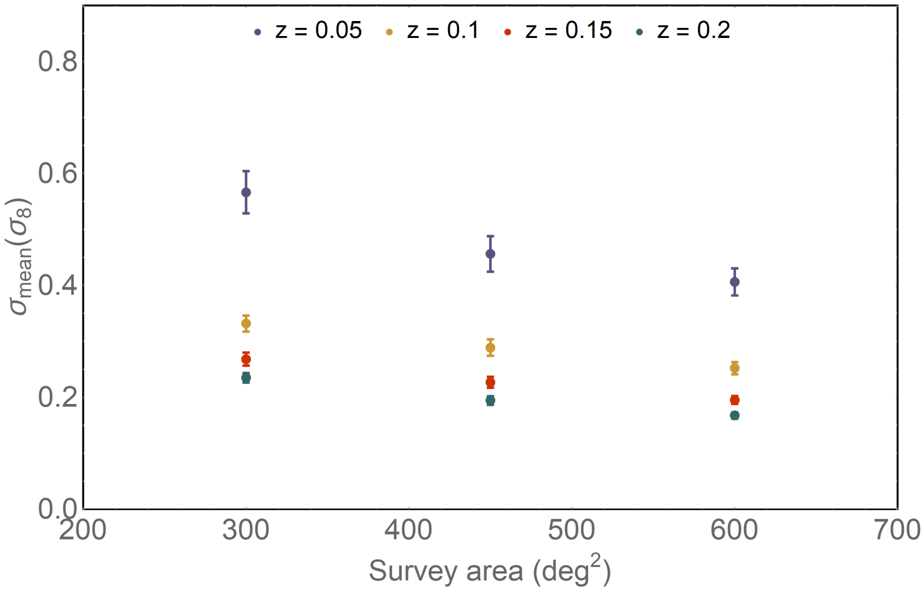

Figure 4.16: The standard deviation of σ_8 with 2σ error bars as a function of the survey area, for the different redshift limits indicated.

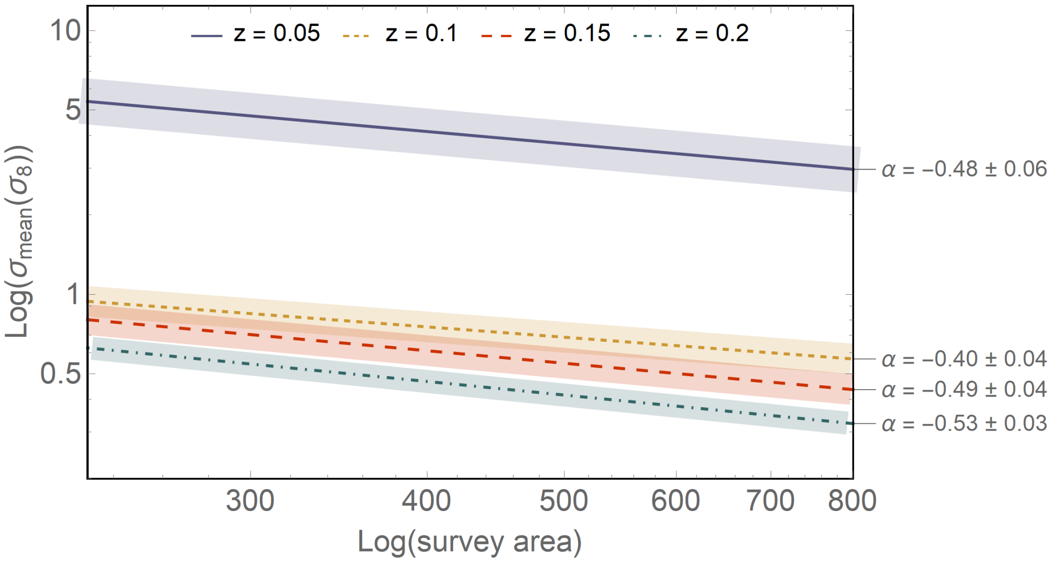

Figure 4.17: Log-log analysis of the error for σ_8 for different redshift limits as a function of the survey area performed by taking the average of the inclinations of all the versions.

4.4 The case of γ

In order to make predictions on the γ parameter, we performed the same estimation process as we did to σ_8, but now making γ free while all the other parameters are fixed. Although it would be worth reproducing also the analysis we did to σ_8 based on the Fisher matrix, the γ estimation process is a little trickier, as its likelihood curve is not as similar to a Gaussian distribution as it is in the case of σ_8. In Figure (4.18) one can see an example of constraints on γ for a subcatalog covering 600 deg^2 for 6 years, reaching $z = 0.05$. Fortunately, the more signal we have, the more the likelihood curve seems like Gaussian, as it is shown in Figure (4.19). The area covered in this case is the same of Figure (4.18), and the duration is also 6 years, but it is reaching $z = 0.15$, adding more supernovae to the sample.

We studied how the constraints on γ depend on the survey redshift limit, using the same 11,285-supernovae catalog. Results are shown in Figures (4.20) and (4.21). One can see that, as in the σ_8 case, the gain of information grows until $z = 0.2$. We intend to extend the varying time and varying area analysis to the case of γ in the near future, to be presented in Garcia et al. (2018).

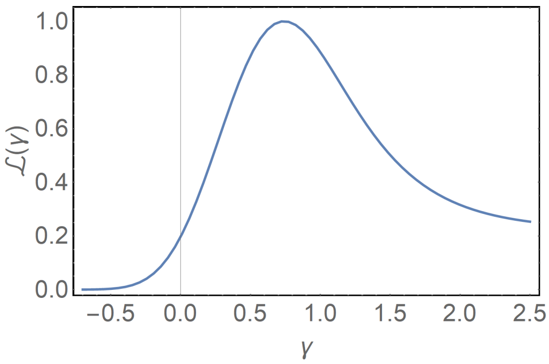

Figure 4.18: γ likelihood curve for a hypothetical survey that covers 600 deg^2, reaches $z = 0.05$ and lasts 6 years.

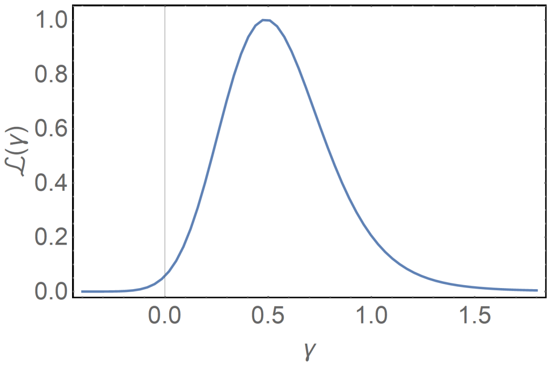

Figure 4.19: σ_8 likelihood curve for a the same hypothetical survey considered in Figure (4.18), but reaching $z = 0.15$ instead.

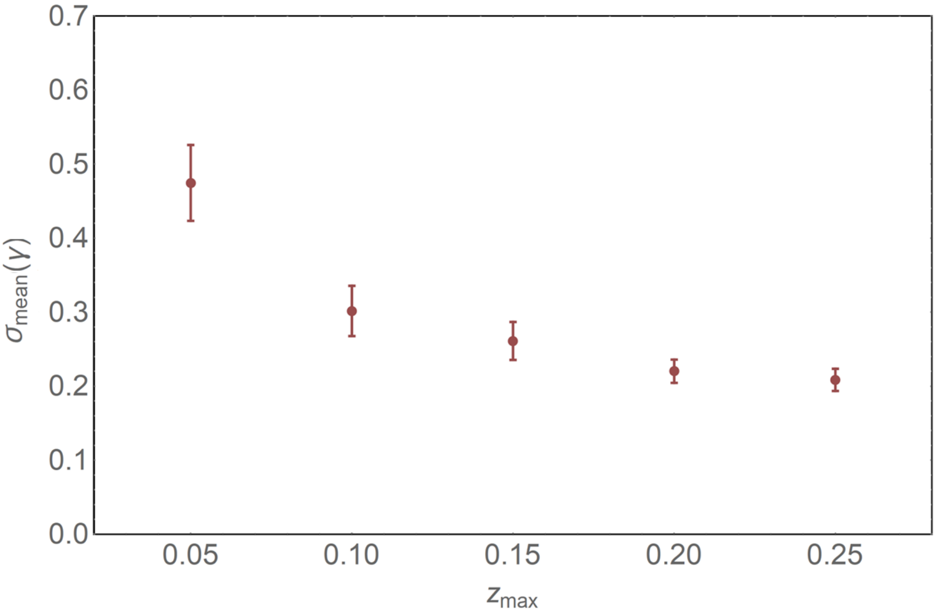

Figure 4.20: The mean standard deviation of γ as a function of the maximum redshift.

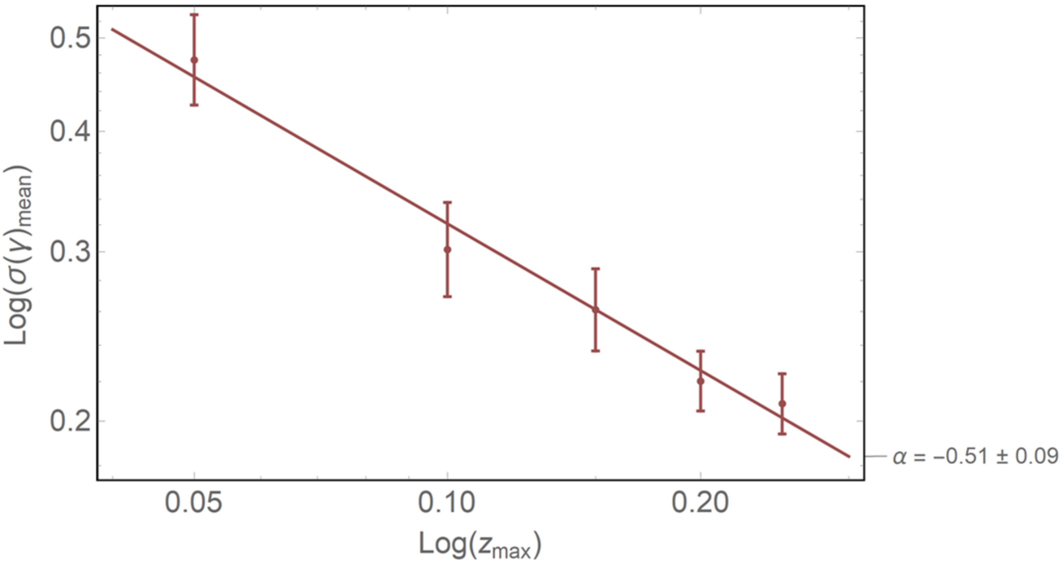

Figure 4.21: The mean standard deviation of γ as a function of the maximum redshift in a log-log scale.

Chapter 5

Conclusions and Future Works

In this work, we showed that the correlation between Type Ia supernova peculiar velocities represents new opportunities to cosmology as it offers constraints on perturbation parameters that background supernova data do not, and provides direct ways of probing the General Relativity theory and the ΛCDM model. Some upcoming surveys, such as the ZTF and LSST, are going to provide an increase of one order of magnitude in the number of low-redshift observed explosions, opening up the possibility of improving cosmological parameter constraints through peculiar velocity studies. However, we do not see in the literature yet (until now) an effort to optimize observations of supernova peculiar velocities. In this work, we compared different observational parameters (area of the sky, survey depth and duration) to understand how they affect perturbation parameters' constraints based on peculiar velocity fields.

Despite what is commonly assumed in the literature, contributions to the overall error budget from supernova peculiar velocities goes beyond $z \lesssim 0.1$; it is possible to gain information on the estimation of σ_8 and γ by going further, until $z \lesssim 0.2$. We showed that, in average, the error on the estimation of σ_8 falls with the square root of the solid angle from which the sky is being observed, which is in accordance with the theoretical prediction. Besides that, the error on the estimation of σ_8 is proportional to the inverse of the number density of supernovae, which is directly proportional to the survey duration. So we showed that we gain information when raising the survey time in the beginning of the survey, but it gets to an apex and the gain of information starts declining after some time, meaning that all the information about the clumpiness of a determined region is getting saturated. Our simulated 11,285-supernova 600-deg^2 catalog, as predicted, was close to (but less negative than) the -1/2 index power law curve in Figure (4.15), meaning that, for this case, looking at this area for a bit longer would be better than changing to another area of the sky.

We are now making predictions on how comparatively well DES, LSST and ZTF will be able to put constraints on σ_8 and γ. The time dedicated for the supernova search with DES is limited to about 10% of the total survey photometric time, covering 30 deg^2 in 5 years for this purpose. LSST will cover nearly 18,000 deg^2 of sky for 10 years, and ZTF will scan 4,000 deg^2 an hour to a depth of 20.5 mag. Despite the huge difference in area covered when comparing DES with LSST and ZTF, our preliminary analysis shows that they all would benefit from staying longer in the same fields than it is intended.

In order to probe those observational parameters with real-survey data, we are employing the SNANA package to simulate and fit Type Ia supernova light curves. Using this software requires survey-specific libraries that include the survey characteristics and strategies. For each supernova observing field, the library includes information about the survey cadence, filters, CCD gain and noise, point spread function, sky background level, zero points and their fluctuations. The zero point encodes exposure time, atmospheric transmission, telescope efficiency and aperture. DES and LSST have their own libraries in SNANA, but these libraries require many adjustments depending on the motivation. We have already performed some simulations based on these surveys and we are now using them to constrain σ_8 and γ. ZTF does not have its own library yet, so we are trying to build it from the very beginning. Results for this analysis are going to complement the ones we already have and represent the core of a paper in preparation: Garcia et al. (2018).

Appendix A

Likelihood x Gaussian Fit

In this appendix, we show a comparison between the results of the likelihood analysis obtained from the real likelihood curves (which can be truncated in $\sigma_8 = 0$), and from the Gaussian fit that was used in all the results shown in Chapter 4. In Figures A.1, A.2 and A.3, we show the differences in the error of σ_8 obtained from the two approaches, as a function of survey area, maximum redshift and survey duration, respectively.

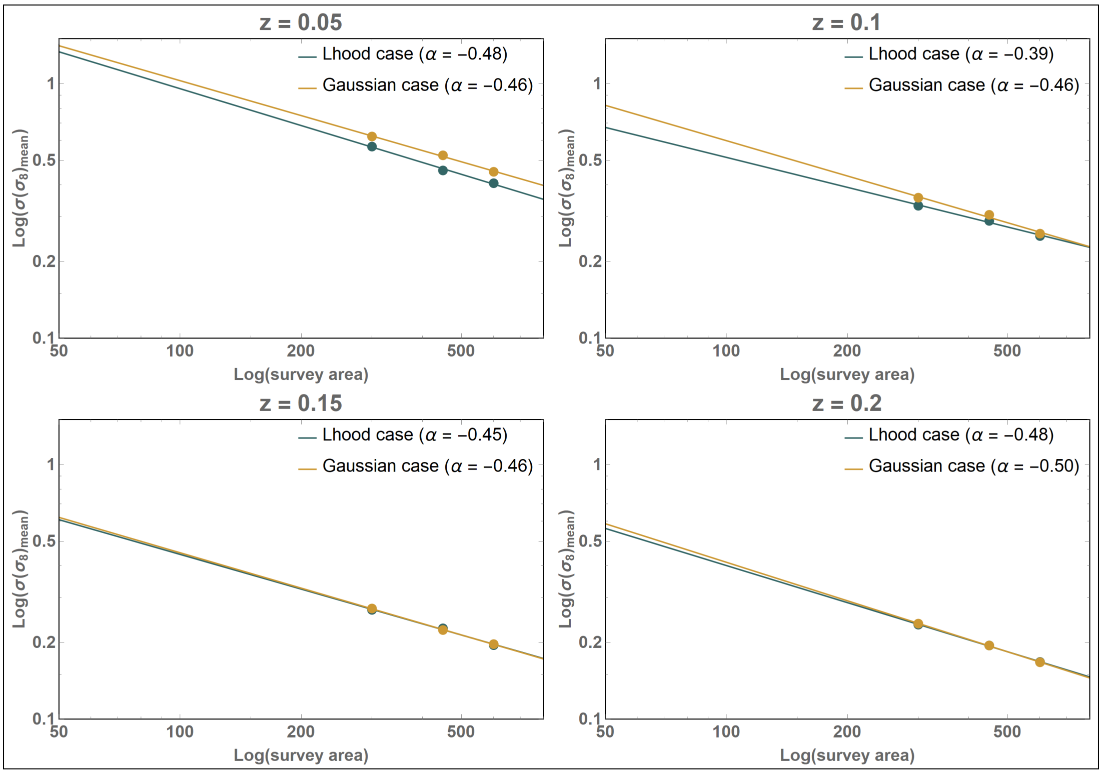

Figure A.1: Comparison between σ_8 estimation errors versus survey area for the analysis using the likelihoods (in blue) and the one using gaussian fits (in yellow).

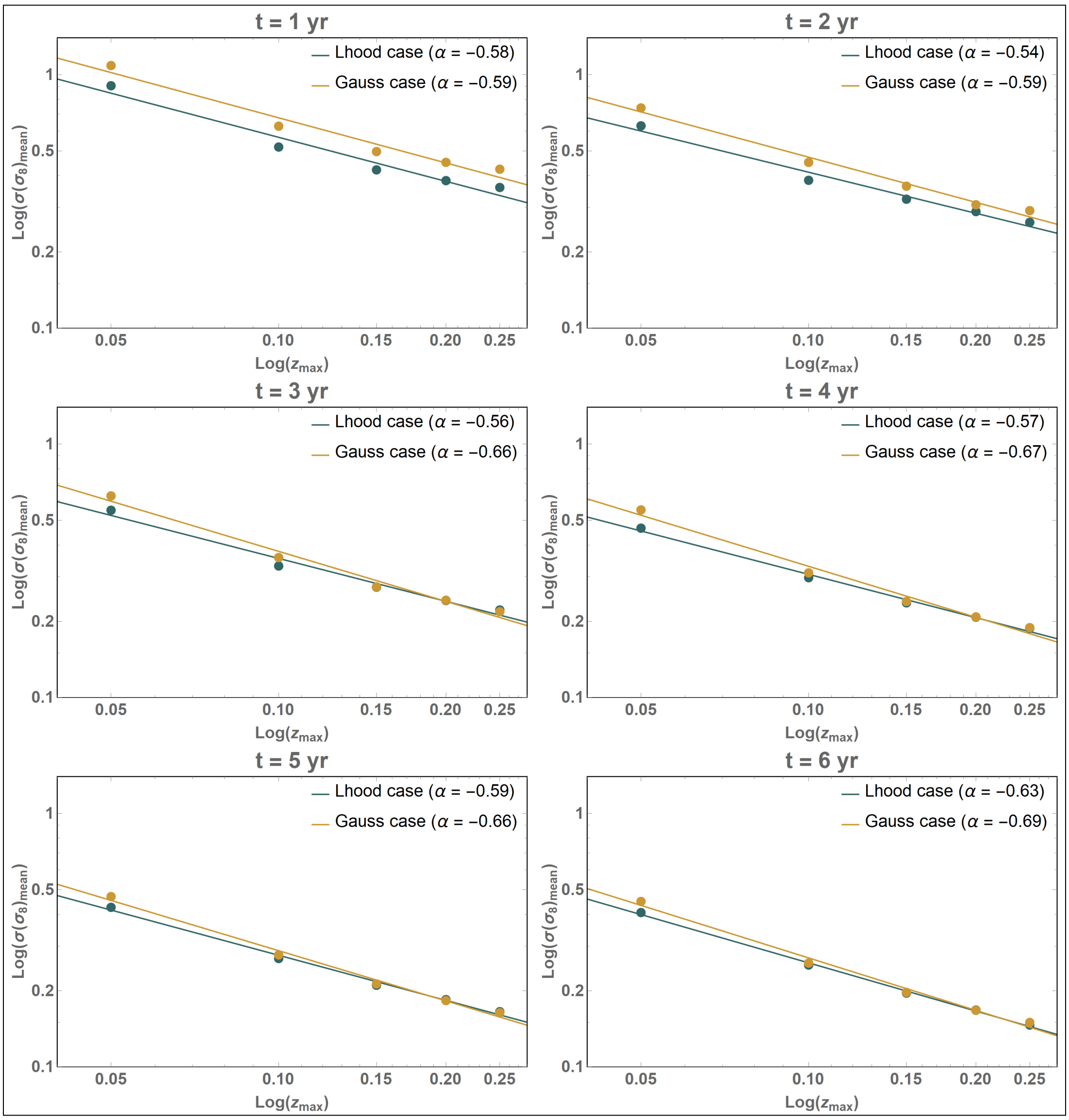

Figure A.2: Comparison between σ_8 estimation errors versus the maximum redshift for the analysis using the likelihoods (in blue) and the one using the gaussian fits (in yellow).

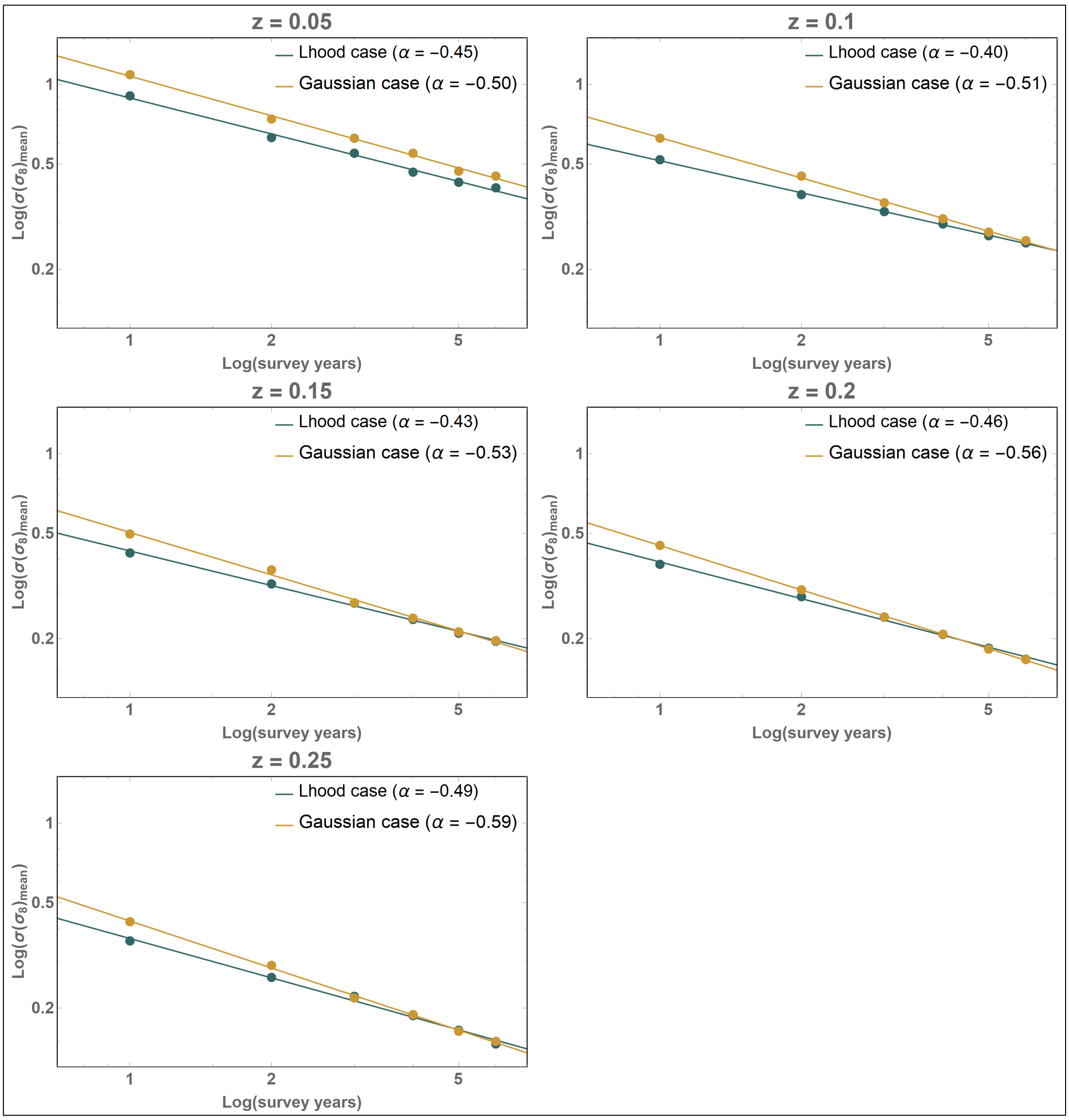

Figure A.3: Comparison between σ_8 estimation errors versus survey years for the analysis using the likelihoods (in blue) and the one using the gaussian fits (in yellow).

Bibliography

Abbott, T., Abdalla, F. B., Aleksic, J., et al. 2016, Monthly Notices of the Royal Astronomical Society, Vol. 460 1

Abell, P. A. 2009, LSST Corporation 1

Anderson, L., Aubourg, E., Bailey, S., et al. 2014, Monthly Notices of the Royal Astronomical Society, Vol. 441, Pg. 24â62 9

Astier, P., Guy, J., Regnault, N., et al. 2006, Astronomy and Astrophysics, Vol. 447, Pg. 31-48 2, 26

Aubourg, E., Bailey, S., Bautista, J., et al. 2014, Physical Review D, Vol. 92 xviii, 11

Bellm, E. 2014, Proceedings of the Third Hot-Wiring the Transient Universe Workshop 1

Bennett, C. L., Larson, D., Weiland, J. L., & Hinshaw, G. 2014, The Astrophysical Journal, Vol. 794, No. 2 39

Bernstein. 2012, The Astrophysical Journal, Vol. 753, No. 2

Betoule, M., Kessler, R., Guy, J., et al. 2014, Astronomy and Astrophysics, Vol. 568, No. A22 xiii, 1, 9, 27, 28

Beutler, F., Blake, C., Colless, M., et al. 2011, Monthly Notices of the Royal Astronomical Society, Vol. 416, Pg. 3017â3032 9

Cappellaro, E., Botticella, M., Pignata, G., et al. 2015, Astronomy and Astrophysics, Vol. 584, No. A62 36

Castro, T., Quartin, M., & Benitez-Herrera, S. 2016, Physics of the Dark Universe, Pg. 66-76 xiii, xiv, 29, 30, 32, 33, 35

Coelho, R., ao, M. C., Reis, R., & Siffert, B. 2015, European Journal of Physics, Vol. 36, No. 1 xii, 21, 22

Coil, A. L. 2012, Invited contribution to be published in Vol. 8 of book Planets, Stars, and Stellar Systems, Springer 16

Coles, P. & Lucchin, F. 2002, Cosmology - The Origin and Evolution of Cosmic Structure (Wiley) 9

Colless, M., Peterson, B., Jackson, C., et al. 2003, arXiv:astro-ph/0306581 xii, 17

Conley, A. 2011, The Astrophysical Journal Supplement Series, Vol. 192, No. 1 xii, xiii, 2, 22, 28

Conley, A., Sullivan, M., Sako, M., et al. 2008, The Astrophysical Journal, Vol. 681, Pg. 482-498

Contreras, C., Hamuy, M., Phillips, M., & Folatelli, G. 2010, The Astronomical Journal, Vol. 139, Pg. 519-539 2

Davis, T., Hui, L., Frieman, J., et al. 2011, The Astrophysical Journal, Vol. 741, No. 1 1, 2

Dodelson, S. 2003, Modern Cosmology (Academic Press) 31

Garcia, K., Quartin, M., & Siffert, B. 2018, in preparation 3, 49, 52

Gjergo, E. 2013, Astroparticle Physics, Vol. 42, Pg. 52-61

Gordon, C., Land, K., & Slosar, A. 2007, Phyical Review Letters, Vol. 99 xiii, 1, 29, 30, 42

Guy, J., Astier, P., Baumont, S., et al. 2007, Astronomy and Astrophysics, Vol. 466, No. 1 22, 26

Hamuy, M., Phillips, M., Suntzeff, N., & Schommer, R. 1996, Astronomical Journal, Vol. 112, Pg. 2391â2397 1, 2, 24

Hicken, M., Challis, P., Jha, S., et al. 2009, The Astrophysical Journal, Vol. 700, No. 1 2

Hogg, D. W. 2000, arXiv:astro-ph/9905116 12

Holtzman, J. A., Marriner, J., Kessler, R., et al. 2008, The Astronomical Journal, Vol. 136, No. 6 2

Howlett, C., Robotham, A., Lagos, C., & Kim, A. 2017, The Astrophysical Journal, Vol. 847, No. 2

Hui, L. & Greene, P. 2006, Physical Review D, Vol. 73 2, 29, 35, 42

Huterer, D., Shafer, D., & Schmidt, F. 2015, Journal of Cosmology and Astroparticle Physics, Vol. 2015 32

Iocco, F., Mangano, G., Miele, G., Pisanti, O., & Serpico, P. D. 2009, Physics Reports, Vol. 472, Pg. 1â76 39

Jha, S., Riess, A., & Kirshner, R. 2007, The Astrophysical Journal, Vol. 659, Pg. 122-148 2, 22

Kessler, R., Becker, A. C., Cinabro, D., et al. 2009a, The Astrophysical Journal Supplement Series, Vol. 185, No. 1 2

Kessler, R., Bernstein, J., Cinabro, D., et al. 2009b, The Astronomical Society of the Pacific, Vol. 121, No. 883 26

Lago, B., Calvao, M., Joras, S., et al. 2011, Astronomy and Astrophysics, Vol. 541, No. A110 22, 25

Lahav, O., Lilje, P., Primack, J., & Rees, M. 1991, MNRAS, Vol. 251, Pg. 128-136 19

Lewis, A., Challinor, A., & Lasenby, A. 2010, The Astrophysical Journal, Vol. 538, Pg. 473-476 35, 39

Percival, W. J. 2013, Lecture given at Post-Planck Cosmology, Ecole de Physique des Houches 16

Perlmutter, S., Aldering, G., Goldhaber, G., et al. 1998, The Astrophysical Journal, Vol. 517, No. 2 1, 24

Planck Collaboration. 2016, Astronomy and Astrophysics, Vol. 594, No. A13 9, 35, 39

Riess, A., Macri, L., Hoffmann, S., & Scolnic, D. 2016, The Astrophysical Journal, Vol. 826, No. 1 9

Riess, A. G., Filippenko, A. V., Challis, P., et al. 1998, The Astronomical Journal, Vol. 116 1, 2, 24

Rodney, S., Riess, A., Strolger, L.-G., et al. 2014, The Astronomical Journal, Vol. 148, No. 1 36

Ross, A., Samushia, L., Howlett, C., et al. 2015, Monthly Notices of the Royal Astronomical Society, Vol. 449, Pg. 835â847 9

Ryden, B. 2003, Introduction to Cosmology (Addison Wesley) 9

Sánchez, J. 2018, Tese de doutorado do programa de doutorado em Astronomia do Observatório Nacional xii, 8

Schneider, P., Ehlers, J., & Falco, E. 1992, Gravitational Lenses (Springer pp 508-509)

Scolnic, D. 2018, The Astrophysical Journal 1

Seo, H. & Eisenstein, D. 2003, The Astrophysical Journal, Vol. 598 41

Spergel, D. 2015, Science, Vol. 347

Springel, V., Frenk, C. S., & White, S. D. M. 2006, Nature, Vol. 440

Sullivan, M., Guy, J., Conley, A., et al. 2011, The Astrophysical Journal, Vol. 737, No. 2 2

Taylor, S. & Gair, J. 2012, Phys. Rev. D 86, 023502 15

Tegmark, M. 1997, Phyical Review Letters, Vol. 79 41

Tegmark, M., Taylor, A., & Heavens, A. 1997, The Astrophysical Journal, Vol. 480, No. 1 41

Wang, L., Goldhaber, G., Aldering, G., & Perlmutter, S. 2003, The Astrophysical Journal, Vol. 590, No. 2 22

Xavier, H. S. 2014, Monthly Notices of the Royal Astronomical Society, Vol. 444

Zhao, W., Broeck, C. V. D., Baskaran, D., & Li, T. G. F. 2011, Phys. Rev. D 83, 023005 15